EVOLUTION OF A METAMORPHIC GRADIENT IN THE FOOTWALL OF THE NORTHERN SNAKE RANGE DETACHMENT, NEVADA

A THESIS
SUBMITTED TO THE FACULTY OF
UNIVERSITY OF MINNESOTA
BY

CHRISTIE JOSUE VILLANUEVA

IN PARTIAL FULFILLMENT OF THE REQUIREMENTS
FOR THE DEGREE OF
MASTER OF SCIENCE

Donna L. Whitney, Christian Teyssier

May 2013

Acknowledgements

I would like to thank my advisors, Donna Whitney and Christian Teyssier, in addition to the STAMP group at the University of Minnesota. Thanks also go to Anette von der Handt for aiding me in the battle for usable microprobe data and to Aude Gébelin for advice in the field.

Dedication

This thesis is dedicated to everyone who helped keep me from freezing to death in the Midwest.

Abstract

The northern Snake Range metamorphic core complex exposes an extensive section of the footwall below a low-angle detachment, and is therefore an ideal location to study the metamorphic evolution of core complex mylonites. Metamorphic grade in the footwall of the northern Snake Range décollement (NSRD) has been observed to increase with structural depth from the chlorite zone to the garnet-staurolite zone. In a transect through footwall schists at Hendry's Creek, textural and mineral composition analyses reveal systematic changes with depth in addition to the metamorphic gradient. Fe/Mg ratios in muscovite are consistent with the metamorphic gradient and increase with depth, whereas Fe/Mg ratios in garnet and chlorite porphyroblasts show the opposite trend. An inflection in chlorite composition occurs in garnet schist ~100 m below the detachment, where Ca zonation patterns in garnet are indicative of more extensive retrogression than in structurally lower samples. Schist at ~100 m below the detachment also contains abundant fluid inclusion planes and shows textural evidence of staurolite breakdown, indicating the presence of fluids at structurally high levels in the footwall. Results suggest that all structural levels sampled experienced amphibolite facies metamorphism, and the structurally highest levels of the footwall were later retrogressed during synextensional, greenschist facies metamorphism localized along the NSRD.

Table of Contents

List of Tables

List of Figures

Introduction

Areas of crustal-scale extension are commonly characterized by the presence of metamorphic core complexes, which consist of an exhumed, ductilely deformed footwall that was juxtaposed against a brittlely deformed hanging wall by a low-angle detachment fault (Fig. 1). As a result of Cenozoic extension, metamorphic core complexes are present throughout the Basin and Range Province of the North American Cordillera (e.g. Coney, 1980) (Fig. 2). The northern Snake Range, a north-south trending range located at the eastern border of central Nevada, is a typical example of a Cordilleran core complex (Fig. 3). The range is bordered by a north-south trending, gently domed detachment fault, the northern Snake Range décollement (NSRD), which exposes a highly metamorphosed footwall mylonite against an unmetamorphosed hanging wall.

The northern Snake Range is an ideal location to study the mechanisms by which core complexes are exhumed, as it has extensive exposures of footwall rocks, is structurally simple, and has a well-described stratigraphy. Additionally, the range has been well-studied; studies in the northern Snake Range have been centered on developing models for the style of detachment initiation, metamorphic conditions, and deformation in the footwall and hanging wall (e.g. Wernicke, 1981; Miller et al., 1983, 1988; Buck, 1988; Wernicke & Axen, 1988; Miller & Gans, 1989; Lee et al., 1991; Lee, 1995; Lewis et al., 1999; Cooper et al., 2010a; Cooper et al., 2010b). This study focuses on the petrology of footwall mylonites in the southern part of the range, exposed in the Hendry's Creek and Hampton Creek areas, and aims to describe the conditions and relative timing of metamorphic and deformational events in the footwall.

A central question addressed by this work is whether the metamorphic gradient in the detachment footwall likely existed prior to extensional deformation and core-complex exhumation or whether it developed during core-complex formation. Metamorphic grade increases with structural depth in the detachment fault zone, from the chlorite zone to the garnet-staurolite zone. Using petrographic observations of textures and analysis of mineral compositions and zoning, I document and interpret the metamorphic history of schists representing ~150 m of the detachment fault zone in order to determine metamorphic conditions in the footwall during core complex evolution.

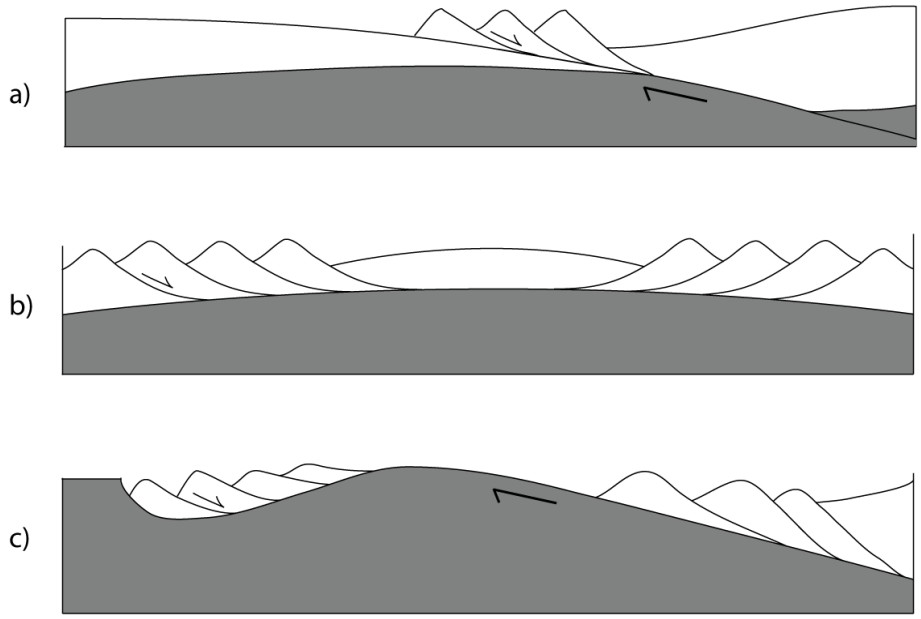

Figure 1: Three models of detachment fault formation in metamorphic core complexes. Shaded areas indicate ductilely-deforming lower crust, and unshaded areas indicate brittlely-deforming upper crust. a) Low angle fault model, wherein the detachment initiates as a shallowly dipping fault that penetrates the lower crust. b) Exhumed brittle-ductile transition model, wherein the detachment initiates as a subhorizontal boundary between the brittle upper crust and ductile lower crust and is exhumed as extension progresses and the crust thins. c) Rolling hinge model, wherein a high angle normal fault

rolls into a subhorizontal orientation as extension progresses and ductile lower crust flows upward to take its place.

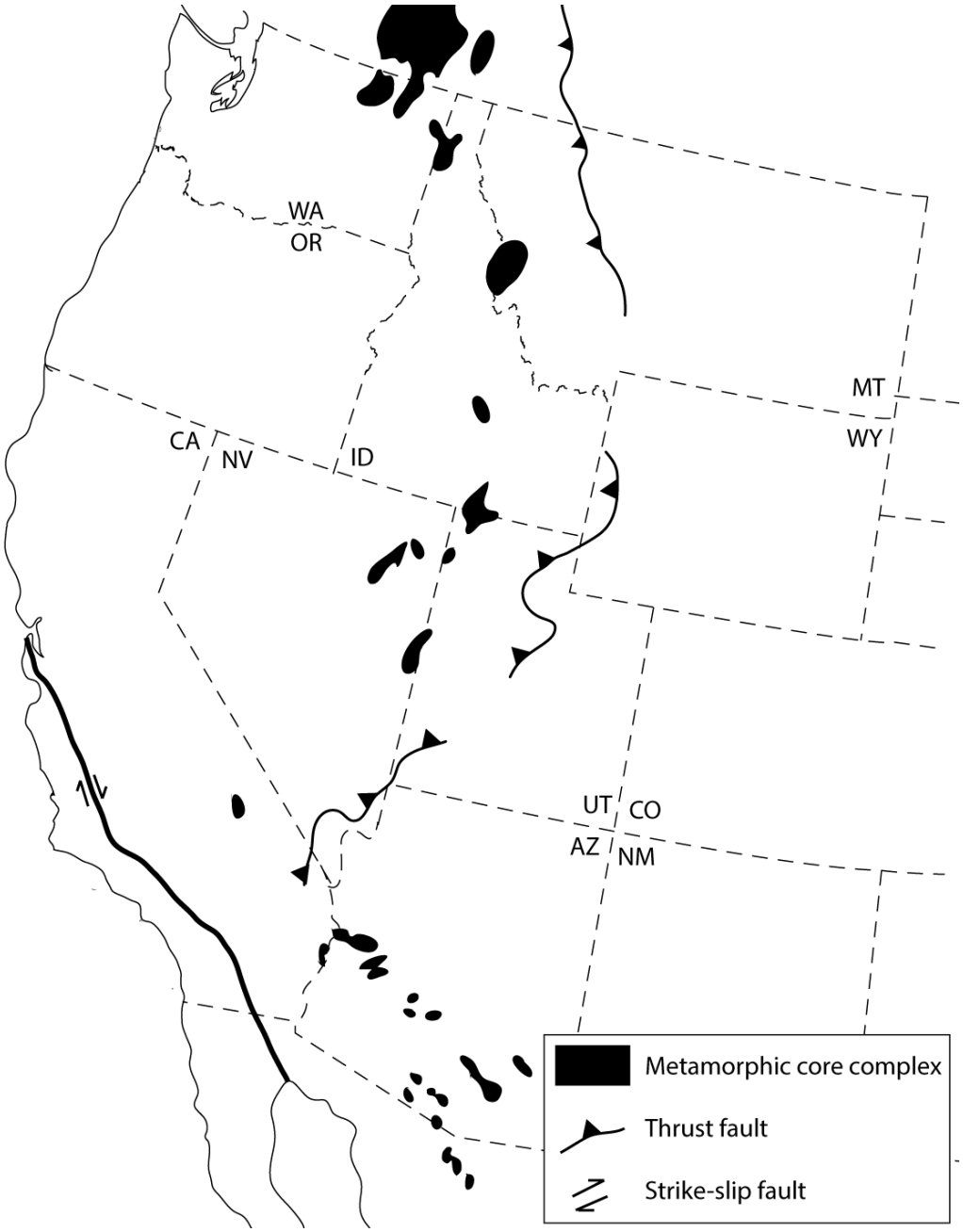

Figure 2: Distribution of Cordilleran metamorphic core complexes. Modified from Armstrong, 1982.

Figure 3: Simplified geological map of the northern Snake Range. Mapping by Gans et al. (1999a,b), Lee et al. (1999a-c), and Miller et al. (1999a,b). Red dot shows location of sampled Hendry's Creek transect.

Geologic Setting

The northern Snake Range is composed of a ~15 km thick Late Precambrian to Late Paleozoic metamorphosed miogeoclinal sequence (Stewart & Poole, 1974) (Fig. 4a). Upper plate strata consist predominantly of extensively faulted Cambrian to Permian limestone and dolomite (Gans et al. 1999a,b; Lee et al. 1999a-c; Miller et al. 1999a,b). In contrast, lower plate rocks are largely made up of L-S tectonites of Upper Precambrian to Lower Cambrian quartzites and pelitic schists. Deformation and metamorphism within the lower plate are heterogeneous; metamorphic grade increases with depth and to the north (Miller et al. 1988), and mylonitization is more developed on the eastern side of the range (Gans & Miller, 1983; Lee et al., 1987). Despite vertical and lateral differences in metamorphism and deformation, minimal stratigraphic omission is observed between the upper and lower plates; units directly above and below the detachment are of approximately the same age (Miller et al., 1983).

Previous Work

As a classic example of a metamorphic core complex, the northern Snake Range has been at the center of studies aiming to model the initiation and style of slip on detachment faults. To explain the stark contrast in metamorphic grade and style of deformation between upper and lower plate rocks, simple shear models frame the NSRD as an extensive, low-angle normal fault that penetrates the entire crust, placing hot, mid-crustal rocks up against cool, brittle upper crustal rocks (Wernicke, 1981, Bartley and Wernicke, 1984) (Fig. 1a).

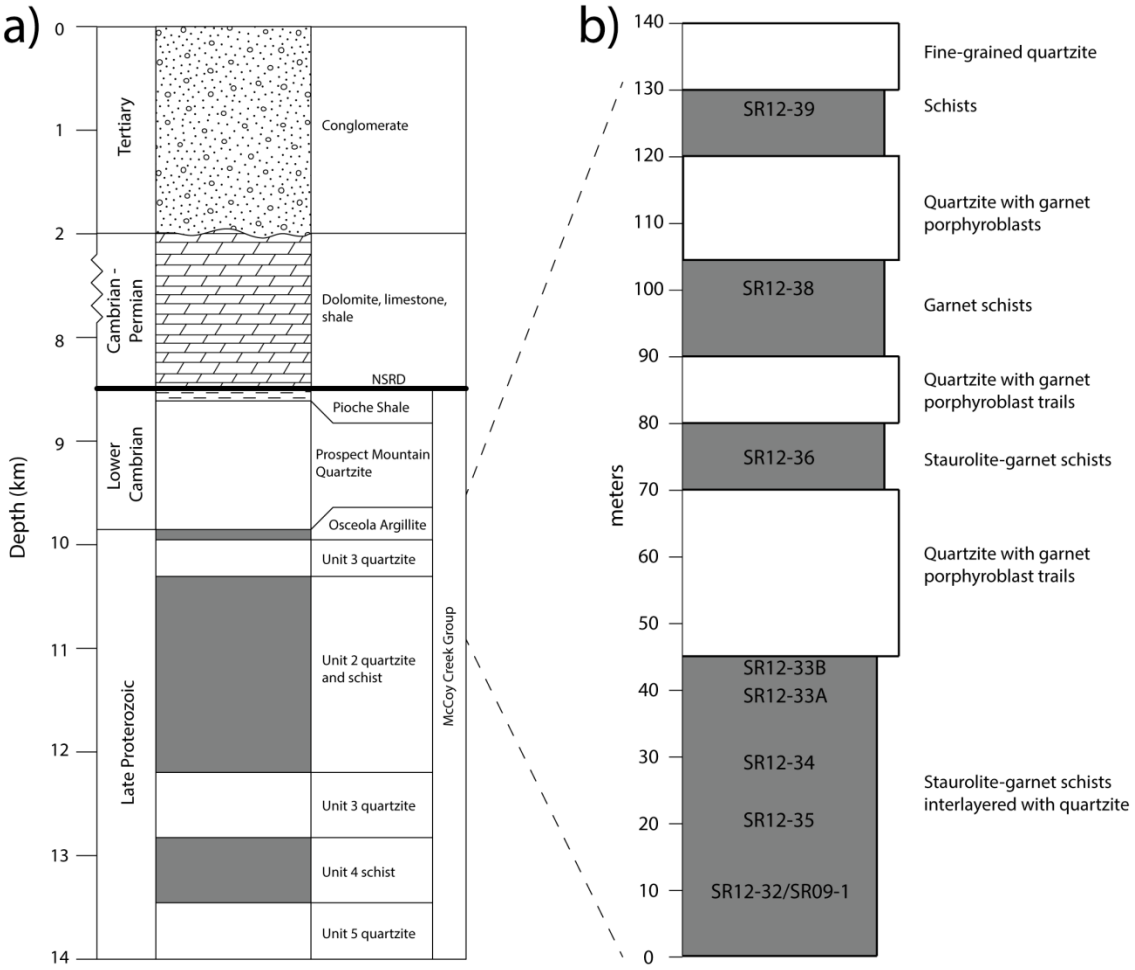

Figure 4: a) Simplified stratigraphic column of the northern Snake Range, showing original stratigraphic thicknesses. Modified from Lee, 1995. b) Sampled transect through Hendry's Creek, showing sample locations.

Alternatively, as the detachment maintains the same stratigraphic position and there is little stratigraphic omission, the NSRD has been interpreted as a sub-horizontal, exhumed brittle-ductile transition between a rising body of hot rock and the overlying crust (Miller et al., 1983; 1999) (Fig. 1b). Whereas the simple shear model demands large amounts of displacement on the order of 60 km (Bartley and Wernicke, 1983), the brittle-ductile

transition model suggests that as little as 10 km of displacement was accommodated on the NSRD, although crustal thinning was substantial (Miller et al., 1983).

A third, "rolling hinge" model has also been proposed, in which a detachment originates as a normal fault then rotates into a sub-horizontal orientation, either in isostatic response to unloading (Spencer, 1984) or as ductile lower crust flows upward beneath the fault (Buck, 1988; Wernicke and Axen, 1988) (Fig. 1c). This interpretation is supported by $^{40}Ar/^{39}Ar$ studies that show cooling ages systematically increasing from 20 to 50 Ma from east to west across the range (Lee, 1995; Lee & Sutter 1999). These results are consistent with exhumation of lower plate rocks along an initial, relatively high-angle, east-dipping fault section.

Deformational History of Footwall Rocks

Miller et al. (1988) described three distinct periods associated with metamorphism: Jurassic pluton emplacement; Cretaceous compression; and Cenozoic extension. Initial intrusion of two-mica granite plutons during Jurassic time was localized in the southern part of the range and resulted in contact metamorphism of lower plate rocks (Miller et al., 1988). During the Cretaceous, as Sevier thrust faulting to the east began, concurrent compression and more widespread intrusion generated gentle folding of the upper plate and amphibolite-grade metamorphism of lower plate rocks (Miller et al., 1988). Cretaceous metamorphism dated at around 80 Ma (Lee and Fischer, 1985; Cooper, 2011b) resulted in a peak staurolite zone mineral assemblage in lower plate schists (Miller et al., 1988). During subsequent Cenozoic extension and associated greenschist

facies metamorphism, sub-horizontal foliation and WNW-ESE stretching lineation with indicators of top to the east shear (Gaudemer & Tapponnier, 1987) were imposed over Cretaceous fabrics (Miller et al., 1988).

Geochronological studies agree that slip on the NSRD itself occurred during multiple distinct periods. Citing fission-track cooling ages, Miller (1999) inferred at least two periods of top to the east slip on the NSRD and concurrent deformation in the upper and lower plate: initial slip in late Eocene to early Oligocene time and rapid slip at ~17 Ma. Thermochronology by Lee (1995) shows three rapid cooling events related to movement on the NSRD in the middle Eocene, late Oligocene, and early Miocene.

Ductile deformation in the lower plate, however, may have stopped before slip on the NSRD ceased. Oxygen and hydrogen isotope ratios in the mylonitic footwall at Hendry's Creek suggest that the NSRD accommodated meteoric fluid flow during extension, allowing meteoric fluids to penetrate upper layers of the footwall and be incorporated in recrystallizing muscovite and quartz. In footwall mylonites, $^{40}Ar/^{39}Ar$ ages for muscovite closest to the detachment are then interpreted as recrystallization ages. The youngest recrystallization age is dated at 23 Ma, which is interpreted as the approximate time that ductile deformation ended (Gébelin et al., 2011).

Thermobarometry

Initial thermobarometric studies were done by Lewis et al. (1999) on amphibolite facies rocks in the Hampton Creek area. Peak metamorphic conditions in this area were calculated at approximately 610° C and 8 kbar. More extensive P-T calculations were

done by Cooper (2010a) on numerous samples from throughout the range, revealing an increase in burial depths from south to north; P-T values in the Hampton Creek area agreed with values from Lewis et al. (1999) at ~8 kbar, but calculated pressures at Hendry's Creek, 3 km south of Hampton Creek, were significantly lower at ~6 kbar. Calculated thermobarometric conditions from both studies also test the validity of detachment initiation models. The exhumed brittle-ductile transition model predicts a maximum burial depth equal to the stratigraphic depth of the unit, which is only ~15 km in the McCoy Creek Group units studied (e.g. Hose & Blake, 1976; Miller et al., 1983, 1988). Pressures calculated from McCoy Creek Group samples are equivalent to burial depths of approximately 30 km, and are inconsistent with the development of the NSRD as a sub-horizontal feature. Additionally, initiation of the NSRD as a low-angle fault would result in a thermobarometric gradient in the ESE-WNW direction of footwall transport; a gradient for which Cooper (2010a) found no evidence.

Petrography of Hendry's Creek Schists

Samples for petrographic and mineral composition analyses were collected from a 140-m long transect through the McCoy Creek Group and Osceola Argillite at Hendry's Creek (Fig. 4b), and further observations were made in the Hampton Creek area to the north. Outcrops at Hendry's Creek consist of meter-scale layers of quartzite and schist, which range in metamorphic grade from greenschist facies at the top of the Hendry's Creek transect to amphibolite facies at deeper levels. The structurally highest sample, SR12-39, is the closest to the detachment (an estimated 60 m below the detachment) and has a

greenschist facies assemblage of quartz + plagioclase + muscovite + chlorite with accessory tourmaline and iron/titanium oxides. Garnet and biotite are introduced to this assemblage in the next deepest sample, SR12-38 (~90 m below the detachment) and staurolite is present in sample SR12-36 (~100 m below the detachment) and below. Schist at all structural levels contains porphyroblasts. Chlorite is present in most samples as 1-5 mm porphyroblasts that range from anhedral to subhedral. The largest chlorite porphyroblasts contain quartz inclusions oriented at a high angle to current foliation (Fig. 5). Muscovite and biotite also occur as porphyroblasts (0.5-2 mm) (Fig. 6), but are less commonly observed and typically do not contain inclusions. In samples with amphibolite facies assemblages, 0.5 to 2 mm garnet and 3-5 cm staurolite are common as fractured, subhedral porphyroblasts. Garnet and staurolite are texturally early as well; in some grains, elongate quartz inclusions occur at high angles to foliation or in slightly curved trails, recording an earlier fabric (Fig. 7). Garnet inclusions in staurolite show no disequilibrium textures and are commonly euhedral, unlike matrix garnet porphyroblasts, which are typically more rounded (Fig. 8).

All porphyroblasts are deformed. Chlorite is locally stretched, and some mica porphyroblasts wrap around garnet and staurolite porphyroblasts. Both garnet and staurolite are fractured and pulled apart, and staurolite is commonly boudinaged (Fig. 9). Additionally, clusters of garnet occur locally, and pulled-apart grain shapes suggest that clustering was early relative to extension (Fig. 10).

All samples, and particularly those from Hampton Creek, exhibit synkinematic greenschist-facies overprinting of higher-grade assemblages; fibrous chlorite, biotite, and

muscovite are present in staurolite boudin necks and in gaps between pulled-apart garnet and staurolite grain fragments (Fig. 9). Retrograde phyllosilicates also occur in pressure shadows of porphyroblasts. Some staurolite boudins in sample SR12-33B are in clear textural disequilibrium, completely surrounded by a rim of chlorite, muscovite, and quartz. Lenses of aligned chlorite aggregates are in contact with and parallel to the axis of extension of these staurolite boudins, suggesting that these chlorite lenses are deformed reaction rims (Fig. 9).

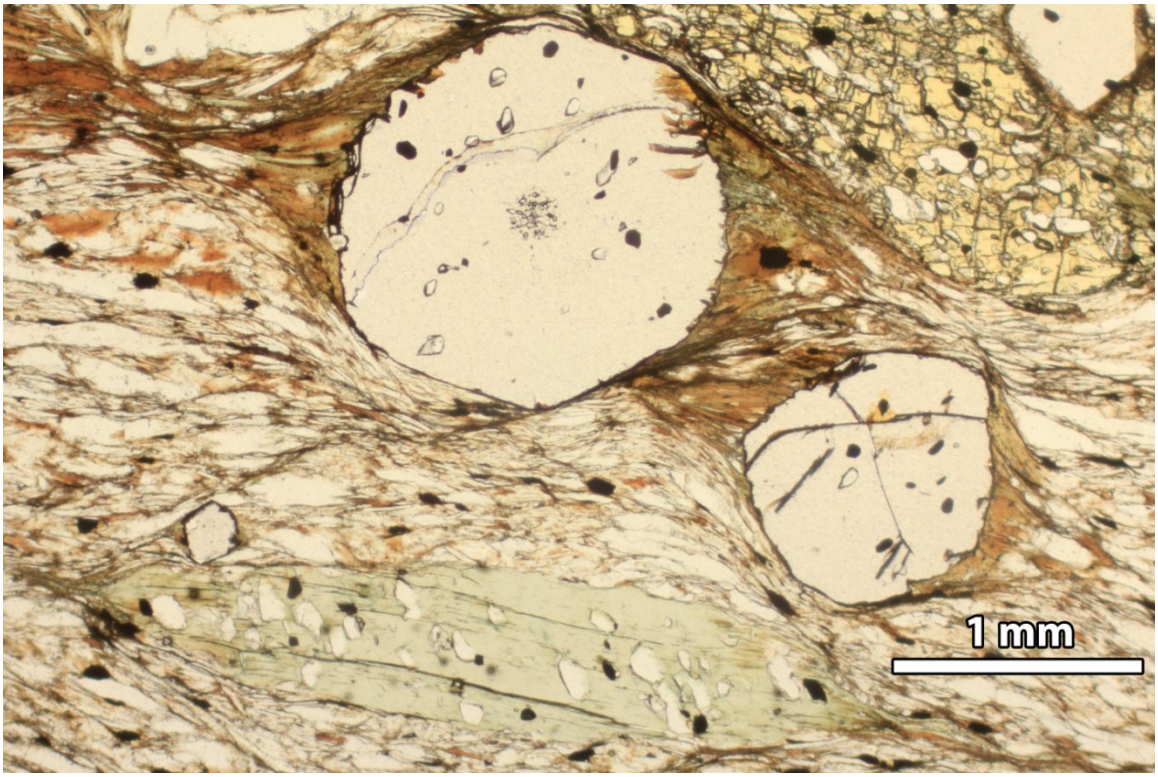

Figure 5: Photomicrograph of chlorite and garnet porphyroblasts. Inclusions in chlorite are aligned at a high angle to foliation.

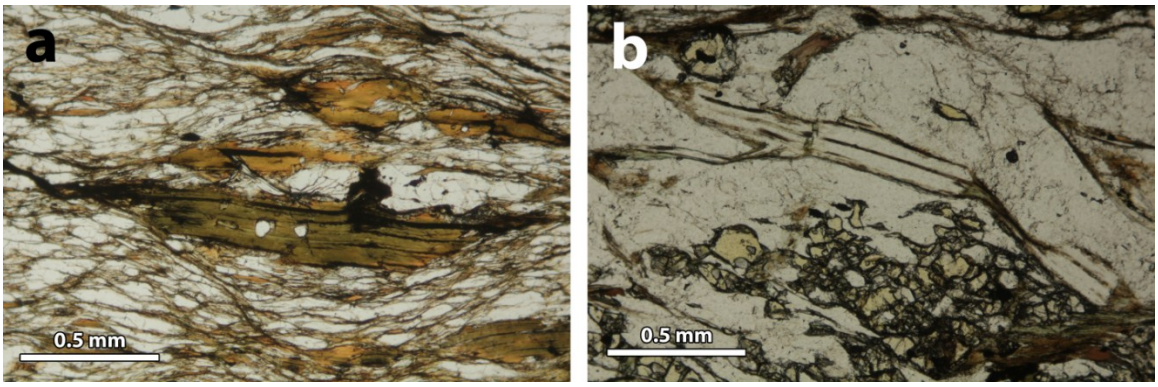

Figure 6: Photomicrograph of a) biotite and b) muscovite porphyroblasts.

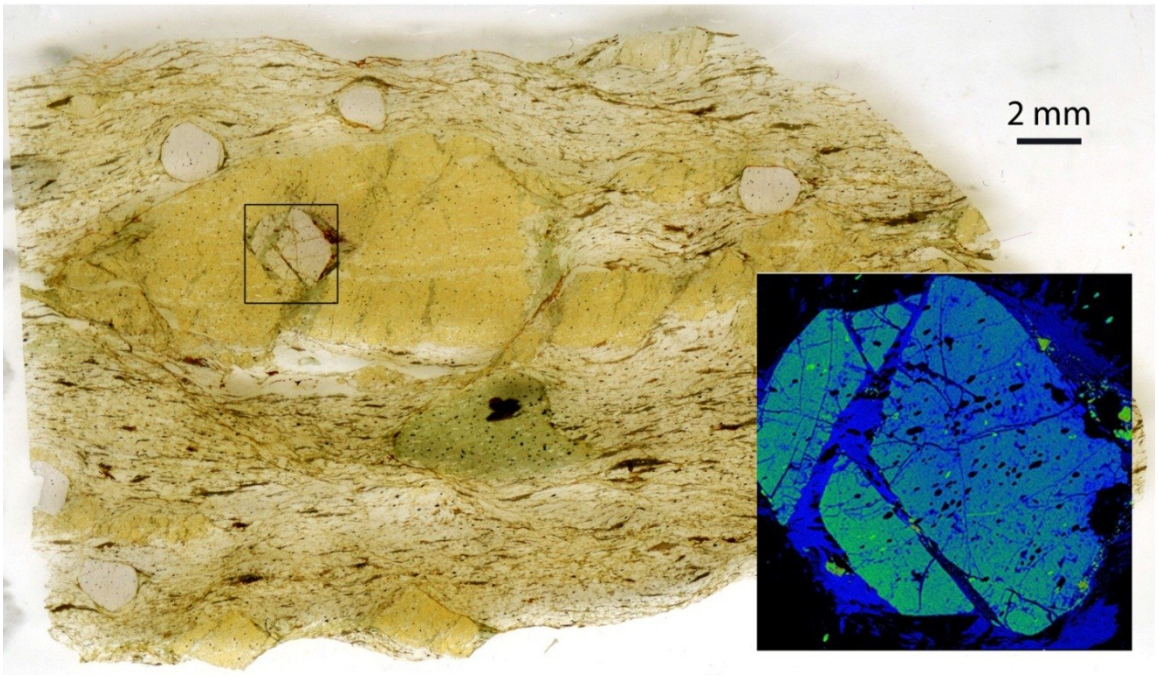

Figure 7: X-ray Fe map of a garnet porphyroblast (inset), showing inclusion trails at a slight angle to foliation, shown in thin section scan.

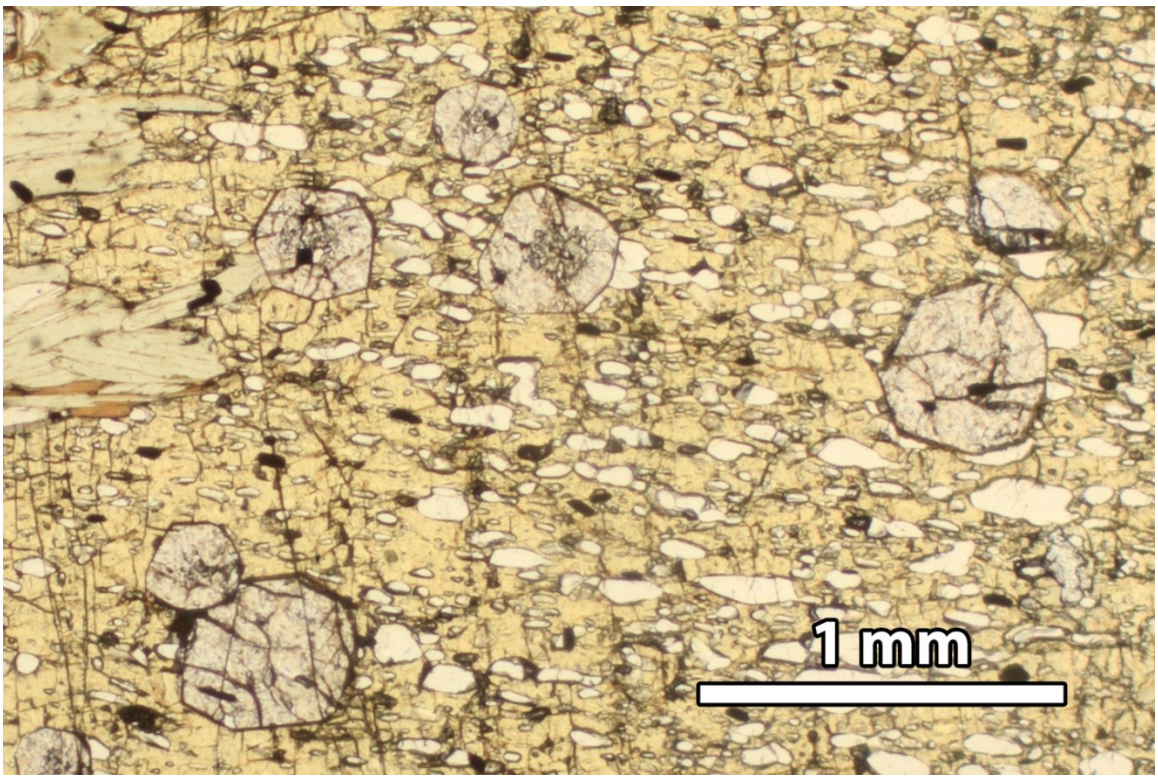

Figure 8: Well-formed garnet inclusions in staurolite. Compare to rounded garnet porphyroblasts in Fig. 5.

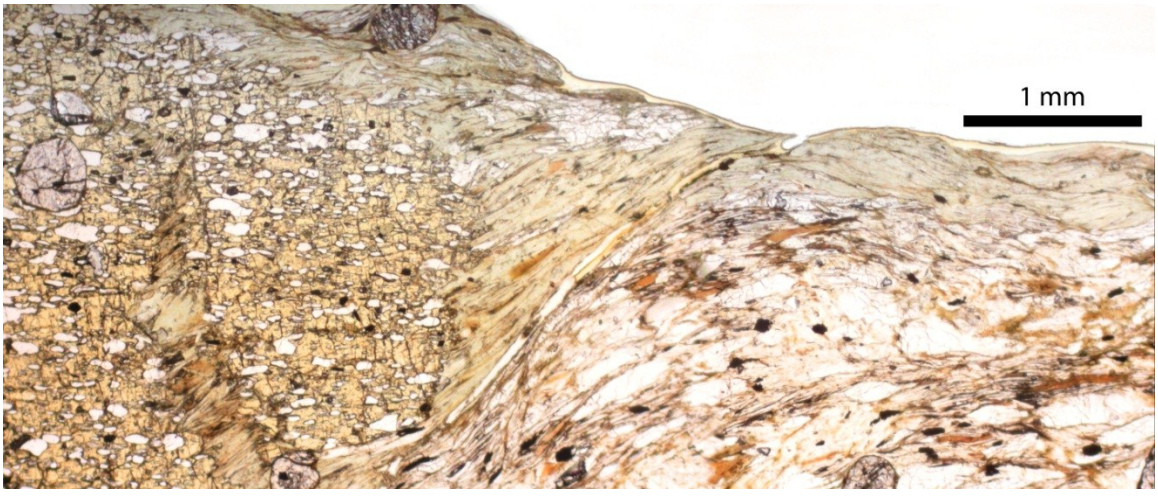

Figure 9: Boudinaged staurolite with texturally late mica growth. Micas occur in boudin necks and lenses.

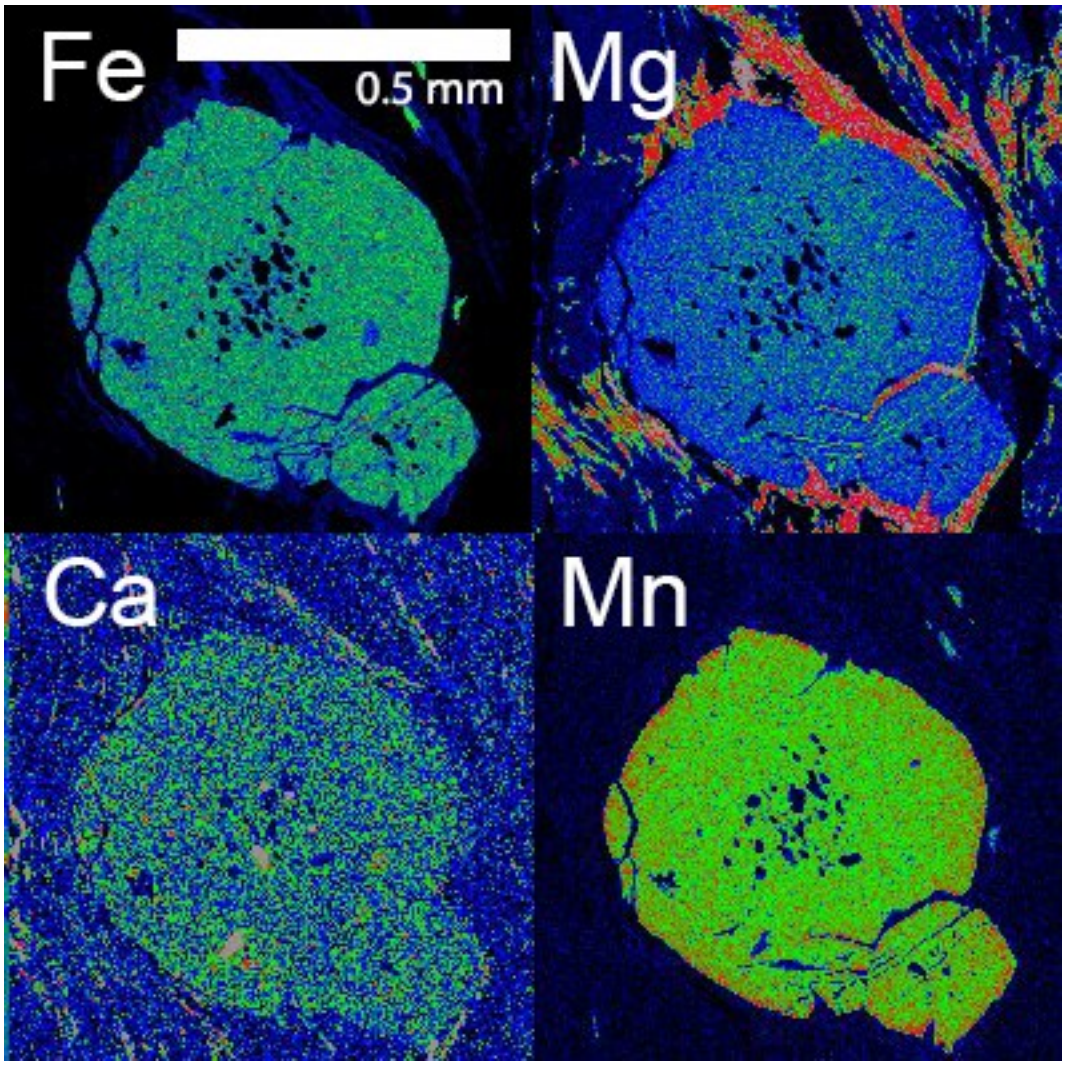

Figure 10: X-ray maps of clustered garnets showing early clustering relative to extensional deformation.

Greenschist facies schists in the top 30 m of the Hendry's Creek transect contain porphyroblasts and textures different from those found in lower sections. Sample SR12-39, the structurally highest greenschist facies sample collected at Hendry's Creek, contains no garnet, staurolite, or biotite, but contains extensively fractured and sheared albite porphyroblasts (Fig. 11). Additionally, this sample contains abundant fluid

inclusion planes at a high angle to foliation (Fig. 11). The second-highest greenschist sample, SR12-38, contains garnet and biotite but no staurolite, and contains ~3-mm lenses of aligned chlorite-muscovite-quartz aggregates similar to those found in SR12-33B (Fig. 12).

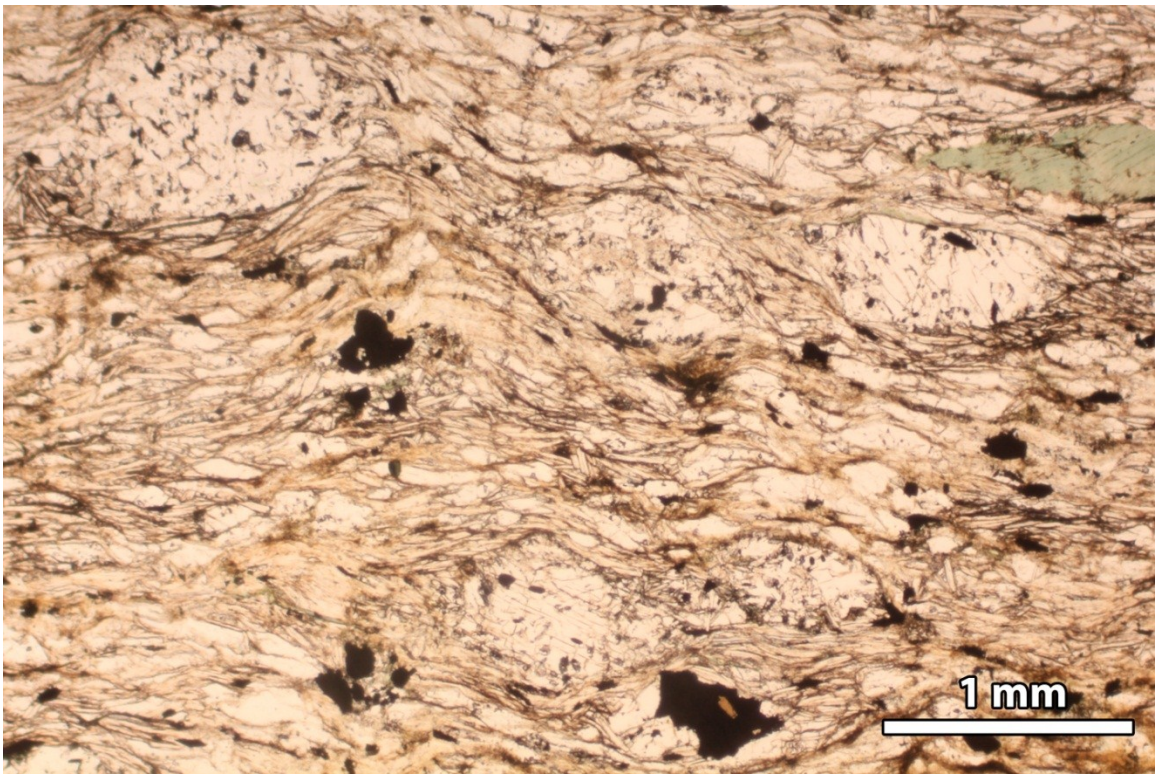

Figure 11: Photomicrograph of features unique to sample SR12-39 showing deformed plagioclase porphyroblasts and fluid inclusion planes at a high angle to foliation.

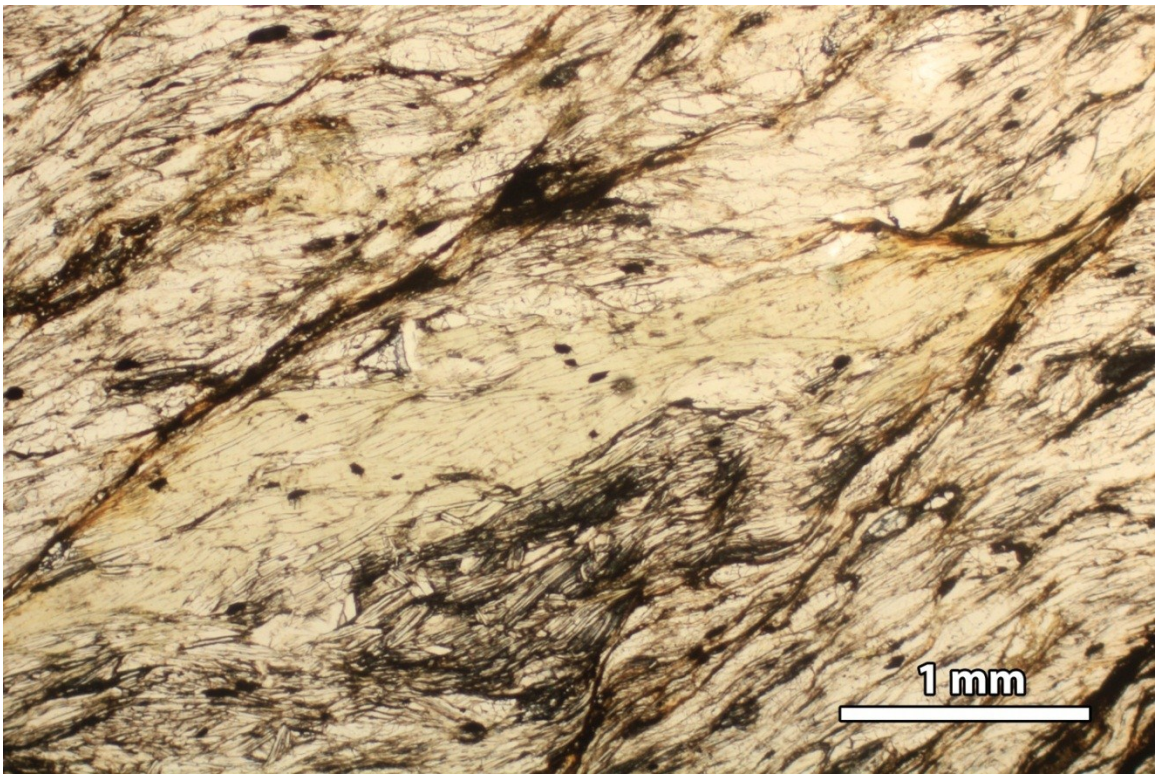

Figure 12: Lens of chlorite and muscovite aggregates in sample SR12-38.

Mineral Compositions

Ten thin sections from Hendry's Creek schists were analyzed to determine compositions of garnet, biotite, chlorite, and muscovite and to characterize garnet zoning. X-ray maps and quantitative composition analyses were obtained using a JEOL JXA-8900 electron microprobe at the University of Minnesota. Quantitative spot analyses were made at 15 kV and 25 nA, with a beam diameter of <1 μm for garnet and plagioclase, and 5 μm for mica. X-ray maps were generated at 15 kV and 100 nA, with a 4 ms/pixel dwell time and 50 μm resolution. A minimum of 3 spot analyses were done on each grain.

Representative mineral compositions are shown in Table 1.

Table 1. Representative mineral compositions.

Mineral	Garnet (core)						
Sample	SR12-38	SR12-36	SR12-33A/B	SR12-34	SR12-35	SR09-1	SR12-32
SiO_2	37.17	37.65	37.16	36.76	37.46	37.80	37.18
Al_2O_3	20.80	21.06	21.24	20.56	20.84	20.50	20.99
TiO_2	0.01	0.02	0.03	0.00	0.02	0.00	0.02
MgO	2.57	2.80	3.32	4.01	3.69	3.67	3.98
FeO	32.57	35.19	36.41	37.39	36.84	34.92	36.02
MnO	4.97	3.85	2.28	1.64	1.42	2.83	1.64
CaO	1.82	0.43	0.21	0.23	0.27	0.23	0.23
Total	99.92	100.99	100.66	100.59	100.54	99.96	100.06
Si	3.01	3.01	2.98	2.97	3.00	3.04	2.99
Al	1.98	1.99	2.01	1.96	1.97	1.94	1.99
Ti	0.00	0.00	0.00	0.00	0.00	0.00	0.00
Mg	0.31	0.33	0.40	0.48	0.44	0.44	0.48
Fe	2.20	2.36	2.44	2.52	2.47	2.35	2.42
Mn	0.34	0.26	0.16	0.11	0.10	0.19	0.11
Ca	0.16	0.04	0.02	0.02	0.02	0.02	0.02
Total	8.00	7.99	8.01	8.06	8.01	7.99	8.01
X_{alm}	0.73	0.79	0.81	0.80	0.81	0.78	0.80
X_{grs}	0.05	0.01	0.01	0.01	0.01	0.01	0.01
X_{prp}	0.10	0.11	0.13	0.15	0.15	0.15	0.16
X_{sps}	0.11	0.09	0.05	0.04	0.03	0.06	0.04
Fe/Mg	7.12	7.05	6.15	5.24	5.59	5.33	5.08

Mineral	Garnet (rim)						
Sample	SR12-38	SR12-36	SR12-33A/B	SR12-34	SR12-35	SR09-1B1	SR12-32
SiO_2	37.47	36.87	36.96	36.97	37.41	37.74	37.76
Al_2O_3	20.93	20.64	20.81	20.44	20.64	20.86	20.70
TiO_2	0.00	0.00	0.02	0.00	0.01	0.08	0.02
MgO	3.20	3.03	2.95	3.21	3.10	3.23	3.19
FeO	35.13	37.24	36.51	37.48	37.06	36.33	37.62
MnO	3.61	1.30	2.85	1.89	2.04	1.92	1.82
CaO	0.51	0.23	0.26	0.26	0.27	0.32	0.26
Total	100.84	99.31	100.36	100.24	100.55	100.47	101.37
Si	3.00	3.01	2.99	3.00	3.01	3.03	3.02
Al	1.98	1.98	1.98	1.95	1.96	1.97	1.95
Ti	0.00	0.00	0.00	0.00	0.00	0.00	0.00
Mg	0.38	0.37	0.36	0.39	0.37	0.39	0.38
Fe	2.36	2.54	2.47	2.54	2.50	2.44	2.51
Mn	0.24	0.09	0.20	0.13	0.14	0.13	0.12
Ca	0.04	0.02	0.02	0.02	0.02	0.03	0.02
Total	8.01	8.00	8.02	8.03	8.01	7.98	8.01
X_{alm}	0.78	0.84	0.81	0.82	0.82	0.82	0.83
X_{grs}	0.01	0.01	0.01	0.01	0.01	0.01	0.01
X_{prp}	0.13	0.12	0.12	0.13	0.12	0.13	0.13
X_{sps}	0.08	0.03	0.06	0.04	0.05	0.04	0.04
Fe/Mg	6.17	6.89	6.95	6.54	6.70	6.31	6.61

Mineral	Chlorite (pressure shadows)					Chlorite (porphyroblasts)							
Sample	SR12-39	SR12-38	SR12-36	SR12-33A/B	SR12-34	SR09-1	SR12-32	SR12-39	SR12-38	SR12-36	SR12-34	SR09-1B	SR12-32
SiO_2	25.55	25.14	26.14	23.93	25.06	24.70	25.13	24.86	23.33	24.68	24.89	24.82	24.53
Al_2O_3	23.81	21.88	22.02	23.77	23.05	22.99	24.97	24.37	22.90	24.04	23.91	24.15	23.87
TiO_2	0.08	0.07	0.33	0.08	0.07	0.06	0.08	0.04	0.05	0.09	0.14	0.04	0.08
MgO	19.32	13.45	11.71	13.95	14.24	14.29	16.67	19.12	14.24	17.03	16.76	16.53	16.65
FeO	19.11	26.21	26.80	27.12	25.97	26.63	23.75	20.19	25.10	23.91	23.80	22.55	23.16
MnO	0.01	0.16	0.08	0.08	0.07	0.07	0.02	0.08	0.11	0.08	0.06	0.06	0.00
CaO	0.06	0.11	0.03	0.00	0.14	0.02	0.03	0.01	0.05	0.04	0.02	0.02	0.02
Na_2O	0.00	0.08	0.00	0.03	0.03	0.01	0.00	0.00	0.04	0.01	0.02	0.01	0.00
K_2O	0.12	0.38	2.17	0.09	0.22	0.34	0.01	0.04	0.10	0.01	0.01	0.10	0.00
Total	88.07	87.49	89.28	89.06	88.86	89.12	90.67	88.70	85.91	89.88	89.61	88.28	88.31
Ca	0.01	0.03	0.01	0.00	0.03	0.00	0.01	0.04	0.00	0.66	0.00	0.01	0.00
Si	5.18	5.35	5.50	5.01	5.22	5.16	5.05	5.03	5.08	5.03	5.08	5.11	5.07
Fe	3.24	4.66	4.72	4.75	4.53	4.65	3.99	3.42	4.45	4.07	4.06	3.88	4.00
Mg	5.83	4.27	3.67	4.36	4.43	4.45	5.00	5.77	4.63	5.17	5.10	5.07	5.13
Al	5.68	5.49	5.46	5.87	5.66	5.66	5.91	5.81	5.80	5.77	5.75	5.86	5.81
Ti	0.01	0.01	0.05	0.01	0.01	0.01	0.01	0.01	0.01	0.01	0.02	0.01	0.01
Mn	0.00	0.03	0.01	0.01	0.01	0.01	0.00	0.01	0.02	0.01	0.01	0.01	0.00
Na	0.00	0.03	0.00	0.01	0.01	0.01	0.00	0.00	0.00	0.01	0.01	0.00	0.00
K	0.03	0.10	0.58	0.02	0.06	0.09	0.00	0.01	0.01	0.00	0.00	0.03	0.00
Total	19.99	19.96	20.01	20.06	19.97	20.05	19.98	20.10	20.00	20.73	20.03	19.97	20.02
Fe/Mg	0.56	1.09	1.28	1.09	1.02	1.05	0.80	0.59	0.96	0.79	0.80	0.77	0.78

Mineral	Muscovite (pressure shadows)						Muscovite (porphyroblasts)	
	SR12-38	SR12-36	SR12-33A/B	SR12-34	SR12-35	SR12-32	SR12-38	SR12-34
SiO_2	43.76	44.79	45.73	46.06	45.18	43.65	46.06	45.87
Al_2O_3	34.66	35.06	36.65	36.49	36.89	35.70	37.32	36.69
TiO_2	0.34	0.35	0.37	0.42	0.48	0.54	0.28	0.41
MgO	0.60	0.84	0.67	0.59	0.56	1.43	0.51	0.59
FeO	1.06	1.46	1.34	1.30	1.25	3.90	0.97	1.13
MnO	0.02	0.02	0.00	0.03	0.02	0.01	0.00	0.00
CaO	0.01	0.03	0.07	0.00	0.06	0.15	0.00	0.12
Na_2O	1.22	0.93	1.57	1.77	1.83	2.23	1.35	1.86
K_2O	8.61	9.21	8.88	8.06	8.68	7.63	9.25	8.13
Total	90.29	92.68	95.28	94.72	94.96	95.23	95.75	94.78
Si	3.05	3.05	3.03	3.05	3.00	2.93	3.03	3.04
Al	2.85	2.82	2.86	2.85	2.89	2.83	2.89	2.86
Ti	0.02	0.02	0.02	0.02	0.02	0.03	0.01	0.02
Mg	0.06	0.08	0.07	0.06	0.06	0.14	0.05	0.06
Fe	0.06	0.08	0.07	0.07	0.07	0.22	0.05	0.06
Mn	0.00	0.00	0.00	0.00	0.00	0.00	0.00	0.00
Ca	0.00	0.00	0.00	0.00	0.00	0.01	0.00	0.01
Na	0.17	0.12	0.20	0.23	0.24	0.29	0.17	0.24
K	0.77	0.80	0.75	0.68	0.74	0.65	0.78	0.69
Total	6.97	6.98	6.97	6.96	7.02	7.10	6.99	6.97
X_{mu}	0.82	0.87	0.79	0.75	0.76	0.69	0.82	0.74
X_{pa}	0.18	0.13	0.21	0.25	0.24	0.31	0.18	0.26
Fe/Mg	0.99	0.98	1.12	1.24	1.26	1.53	1.08	1.09

Mineral	Biotite (pressure shadows)						Biotite (porphyroblasts)				
Sample	SR12-36	SR12-33A/B	SR12-34	SR12-35	SR09-1	SR12-32	SR12-36	SR12-33A/B	SR12-34	SR09-1	SR12-32
SiO_2	35.21	35.63	35.09	36.28	36.30	35.59	34.78	36.29	35.86	36.87	35.59
Al_2O_3	19.41	19.95	20.70	20.95	20.10	20.65	19.44	20.21	19.85	20.05	20.65
TiO_2	1.64	1.95	1.21	1.34	1.50	1.24	1.41	1.49	1.86	1.52	1.24
MgO	9.69	8.45	10.59	10.72	10.67	10.21	11.32	10.76	10.52	11.15	10.21
FeO	18.97	21.08	20.44	16.67	19.10	18.61	19.51	17.76	18.75	17.12	18.61
MnO	0.02	0.07	0.07	0.01	0.04	0.07	0.06	0.06	0.04	0.02	0.07
CaO	0.15	0.03	0.07	0.09	0.08	0.12	0.08	0.03	0.02	0.09	0.12
Na_2O	0.25	0.21	0.26	0.31	0.42	0.42	0.18	0.65	0.55	0.24	0.42
K_2O	8.18	9.60	8.60	9.25	8.70	8.16	7.59	8.91	8.51	8.66	8.16
Total	93.52	96.96	97.03	95.61	96.90	95.06	94.37	96.17	95.98	95.71	95.06
Si	2.71	2.68	2.62	2.70	2.69	2.68	2.65	2.68	2.68	2.74	2.70
Al	1.76	1.77	1.82	1.84	1.76	1.83	1.75	1.83	1.75	1.75	1.80
Ti	0.09	0.11	0.07	0.08	0.08	0.07	0.08	0.10	0.10	0.08	0.08
Mg	1.11	0.95	1.18	1.19	1.18	1.15	1.29	1.14	1.17	1.23	1.19
Fe	1.22	1.33	1.28	1.04	1.18	1.17	1.24	1.09	1.17	1.06	1.10
Mn	0.00	0.00	0.00	0.00	0.00	0.00	0.00	0.00	0.00	0.00	0.00
Ca	0.01	0.00	0.01	0.01	0.01	0.01	0.01	0.00	0.00	0.01	0.01
Na	0.04	0.03	0.04	0.04	0.06	0.06	0.03	0.09	0.08	0.03	0.07
K	0.80	0.92	0.82	0.88	0.82	0.78	0.74	0.85	0.81	0.82	0.80
Total	7.74	7.80	7.83	7.77	7.79	7.76	7.78	7.77	7.78	7.73	7.75
X_{ann}	0.52	0.58	0.52	0.47	0.50	0.51	0.49	0.49	0.50	0.46	0.48
X_{ph}	0.48	0.42	0.48	0.53	0.50	0.49	0.51	0.51	0.50	0.54	0.52
Fe/Mg	1.10	1.40	1.08	0.87	1.00	1.02	0.97	0.96	1.00	0.86	0.92

Garnet

X-ray maps of garnets show Mn and Mg zoning in all samples (Fig. 13). Cores of garnets show relatively flat Mg zonation profiles, but some grains exhibit a subtle increase in Mg from core to rim, from X_{prp} = 0.14 to 0.15 (Fig. 14). Rims are more distinctly zoned; in most grains analyzed, a sharp decrease in Mg begins at the outer ~300 um of the grain. Similarly, garnet cores are either unzoned or decrease in Mn from core to rim, but Mn increases abruptly in the outer ~30-100 um of the grain. In grains that have been pulled apart, these outermost inflections in both Mn and Mg occur not only at the original grain boundary, but also along the edges of each grain fragment (Fig. 15).

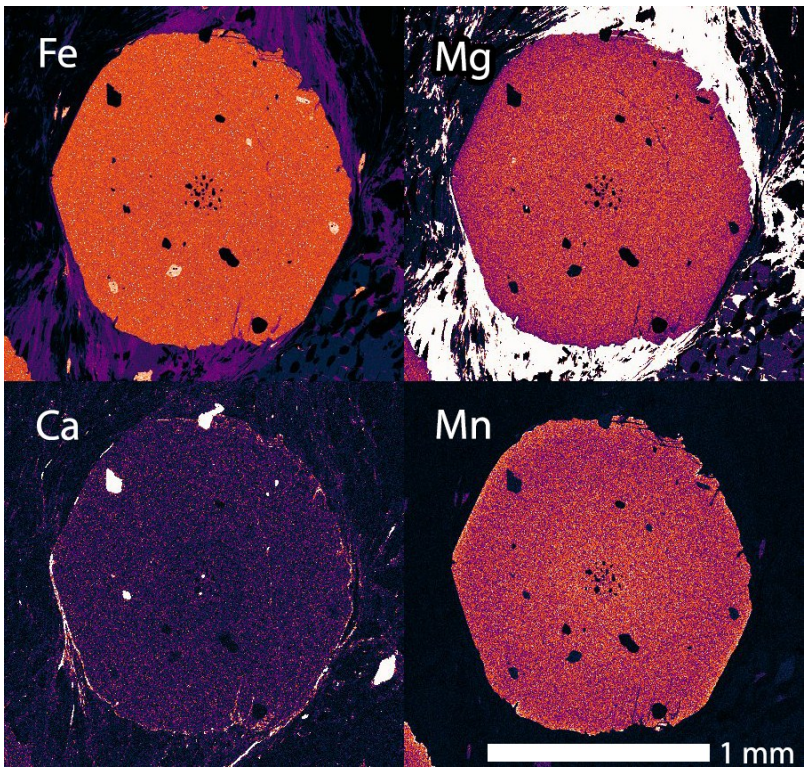

Figure 13: Representative X-ray maps of garnets in the lower 100 m of the Hendry's Creek transect, showing inflections in Mn and Mg compositions at the grain boundary.

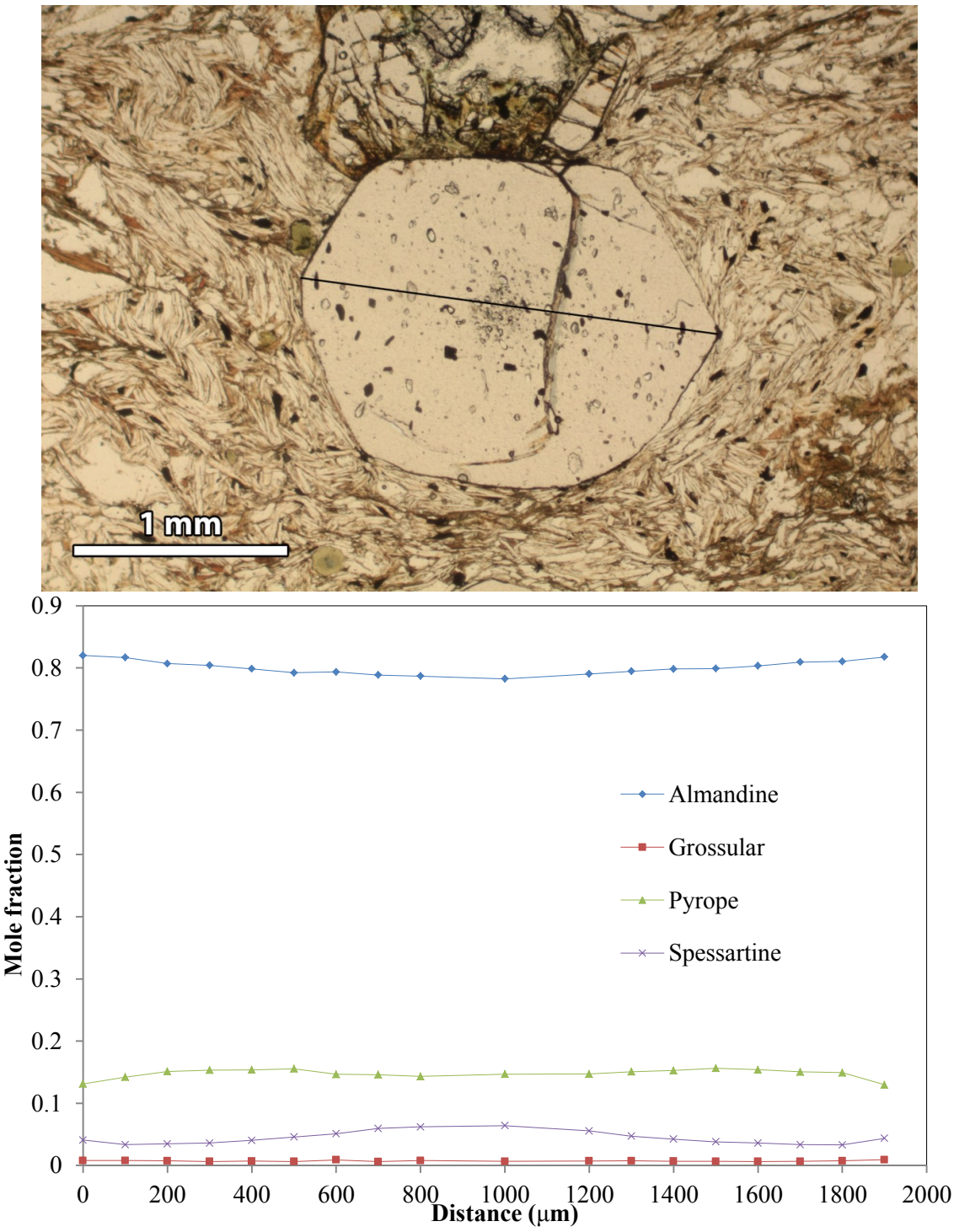

Figure 14: Compositional transect through a representative garnet in SR09-1B1, revealing slightly enriched Mn and depleted Fe and Mg in the core, as well as inflections in Fe, Mg, and Mn at the rim.

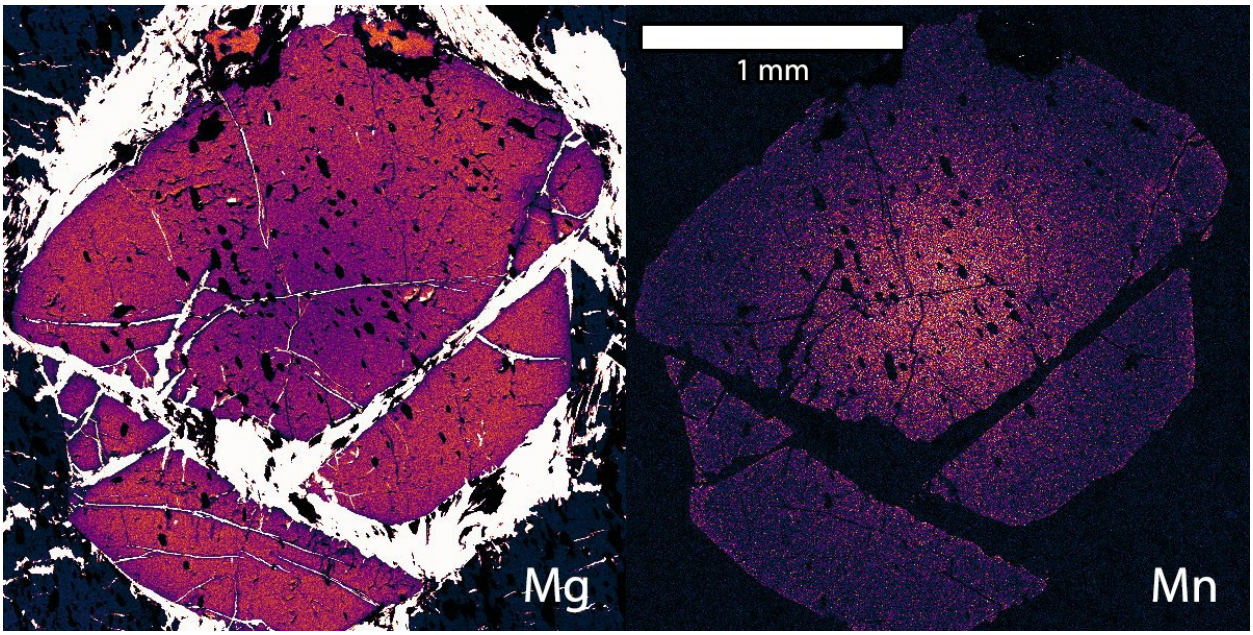

Figure 15: Mg and Mn maps of a pulled-apart garnet, showing compositional inflections at the edge of each grain fragment.

Although Fe and Ca zonation are not clearly distinguishable in most maps, detailed compositional transects through garnets in samples SR12-36 and SR09-1B also reveal a slight, consistent increase in Fe from core to rim (Fig. 14). These detailed transects also confirm that Ca concentrations typically do not significantly change from core to rim. Sample SR12-38, the structurally highest garnet-bearing schist, shows garnet zonation patterns that are unique to the sample (Fig. 16). All garnets in this sample show a sharp boundary between a Ca-enriched core and relatively Ca-depleted, 200-400-um-thick rim. Overall Mg and Mn, and Fe core to rim trends in this sample are similar to those described previously, but the outermost Mg-depleted rims are <100 um thick and consistently thinner than those in other samples. Additionally, the compositional cores of some garnets in this sample are off-center and, in one case, irregularly-shaped (Fig. 17).

Zoning patterns in this garnet seem to be concentric around two different points; this resembles zonation patterns in a Hendry's Creek garnet schist analyzed in a previous EBSD study, which documented the presence of garnet polycrystals. In the Snake Range, garnet polycrystals appear to be morphologically single crystals, but they are comprised of two crystallographically and compositionally distinct garnets (Whitney & Seaton, 2010). As in the previous study, non-concentric zoning is only distinct in the Ca map; however, zoning in the garnet from this study is not as well-defined and shows a Ca-enriched core as opposed to a Ca-depleted core in the previous study.

Additionally, compositions of garnets within one sample, SR12-34, were analyzed to ensure that garnet analyses were representative of the entire sample, and to determine if multiple generations of garnet were present. Three ~2 mm garnets >10 mm apart were analyzed: one rounded grain within a ~5-mm-thick garnet- and staurolite- rich band; one rounded grain outside of the porphyroblasts-rich band; and one euhedral grain in contact with both a staurolite porphyroblast and matrix minerals. No significant compositional differences were observed among the three grains.

Compositional Trends with Depth

Garnet cores and phyllosilicates were analyzed in order to determine trends in mineral composition and metamorphic condition with distance from the detachment. Garnets sampled in the basal 35 m of the Hendry's Creek transect maintain typical compositions of approximately $X_{alm} = 0.80$, $X_{prp} = 0.15$, $X_{sps} = 0.03$, and $X_{grs} = 0.01$; spessartine and

grossular mole fractions consistently increase to $X_{sps} = 0.01$ and $X_{grs} = 0.05$ at the structurally highest occurrence of garnet (~100 m up from the base of the section).

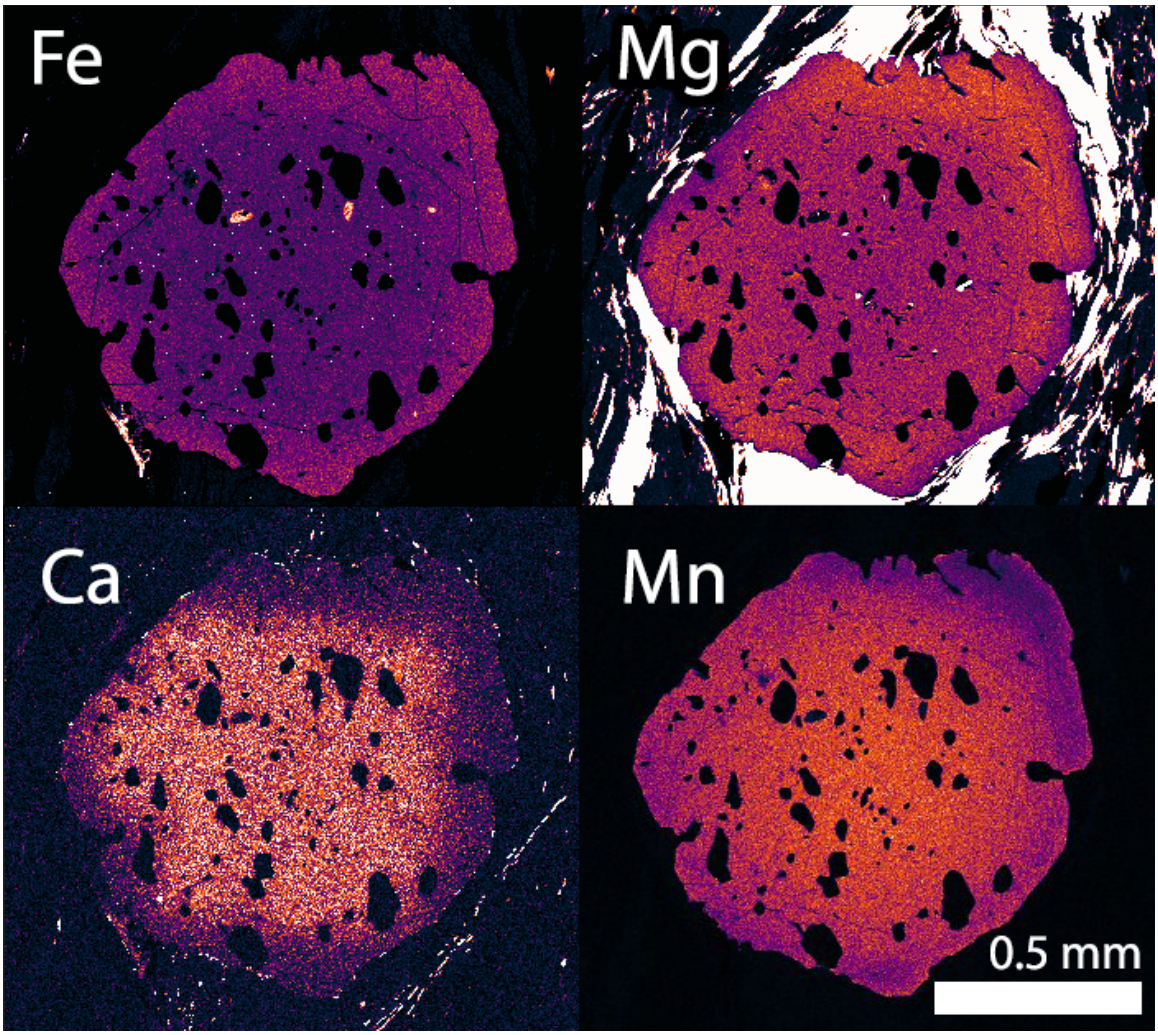

Figure 16: Representative X-ray map of garnets in sample SR12-38, showing a sharply-defined, Ca-enriched core. Fe, Mg, and Mn zonation patterns are similar to those found in lower samples.

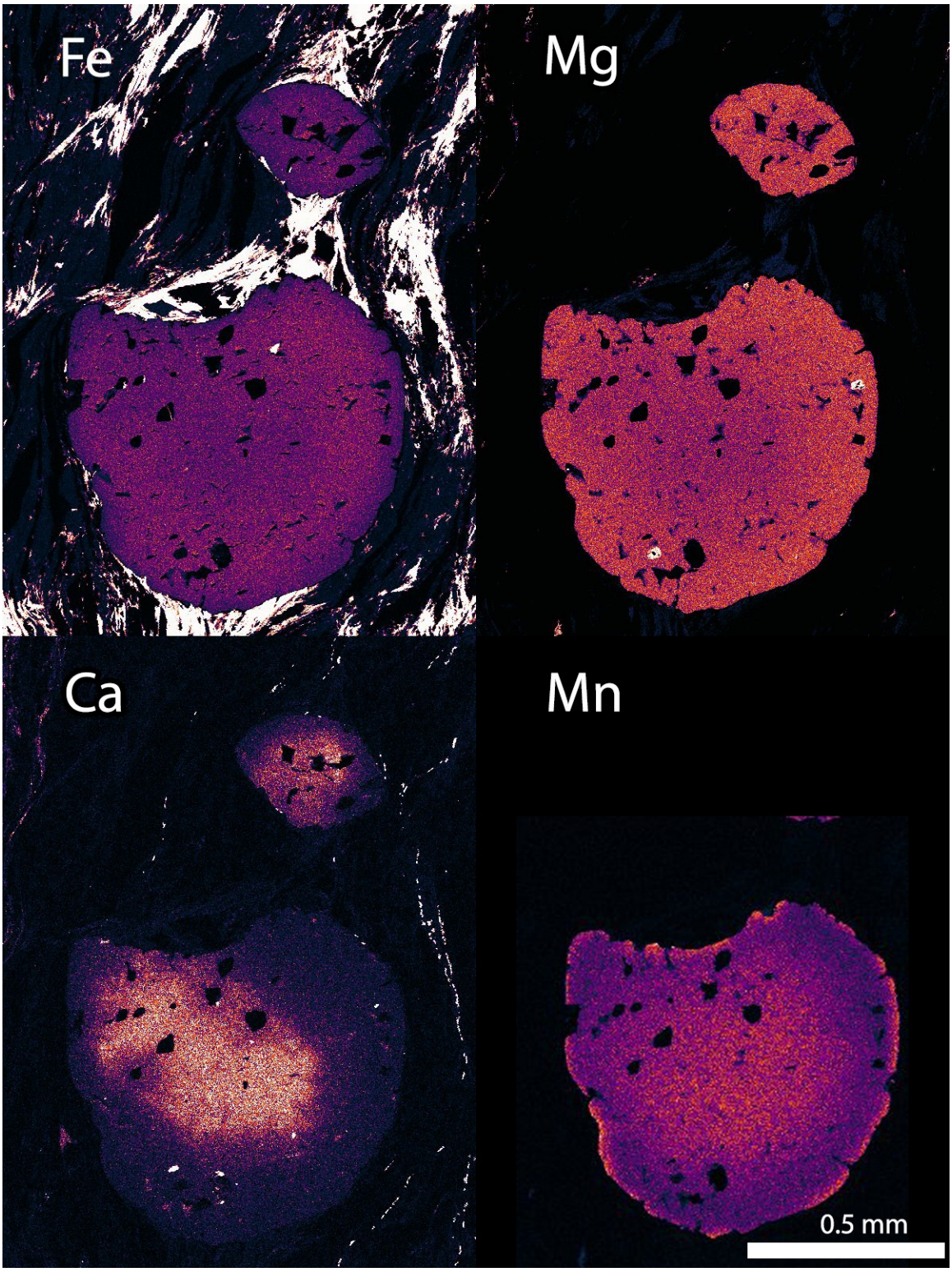

Figure 17: X-ray map of a garnet in sample SR12-38, showing off-center, irregularly-shaped zonation patterns.

Conversely, pyrope and almandine mole fractions decrease to $X_{prp} = 0.10$ and $X_{alm} = 0.72$ at the top (Fig. 18). Fe/Mg ratios in garnet increase from as low as 5.2 at the base to as high as 7.2 at the top of the transect (Fig. 19).

Muscovite also shows a compositional trend with structural distance, decreasing linearly in Fe/Mg ratios from 1.5 at the bottom of the section to .82 at the top, nearest to the detachment (Fig. 20).

Chlorite porphyroblasts and chlorite in pressure shadows were analyzed along the Hendry's Creek transect. A relationship between chlorite composition and depth is not as straightforward as muscovite trends; Fe/Mg ratios in chlorite porphyroblasts increase consistently from ~0.8 at the base of the transect to ~0.9 at the 100-m mark of the transect, then sharply decrease to ~0.5-0.6 at levels closest to the detachment. Two distinct populations of chlorite are present; Fe/Mg ratios of chlorite in pressure shadows are consistently higher than chlorite porphyroblasts and remain constant at ~1 to 100 m, then also drop down to ~0.5-0.6, which is identical to the Fe/Mg ratio in chlorite porphyroblasts from the same sample (Fig. 21). Differences in Al content between chlorite populations are only significant in the basal sample, wherein all analyses of chlorite porphyroblasts show a lower Al composition than chlorite in pressure shadows. Differences in Fe/Mg and Al content between generations of chlorite are generally most distinct at the base of the transect.

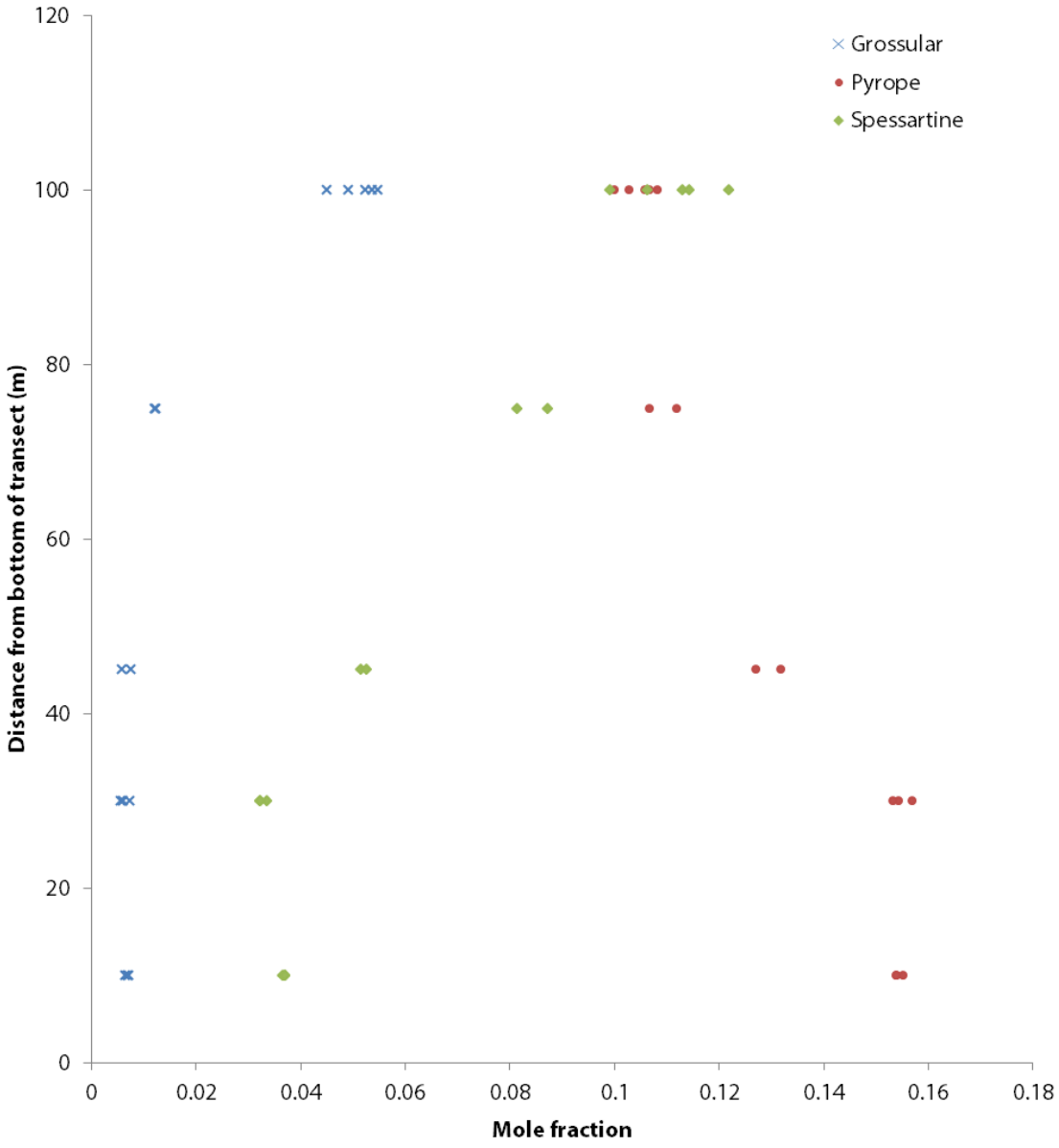

Figure 18: Garnet compositions plotted against structural depth. Spessartine and grossular fractions increase from bottom to top of the transect, while pyrope and almandine decrease.

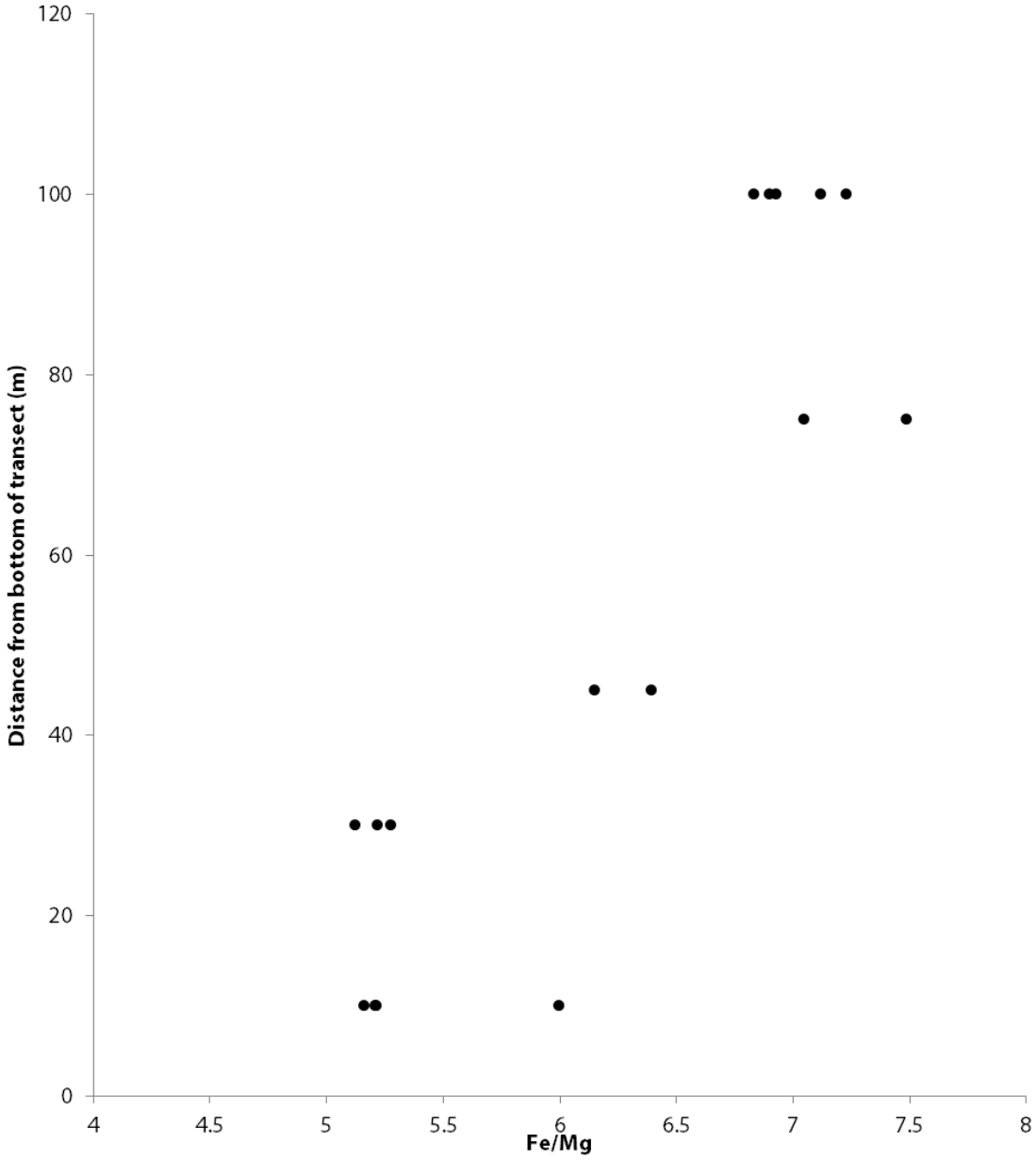

Figure 19: Fe/Mg ratios in garnet plotted against structural depth; Fe/Mg ratios increase from bottom to top of the transect.

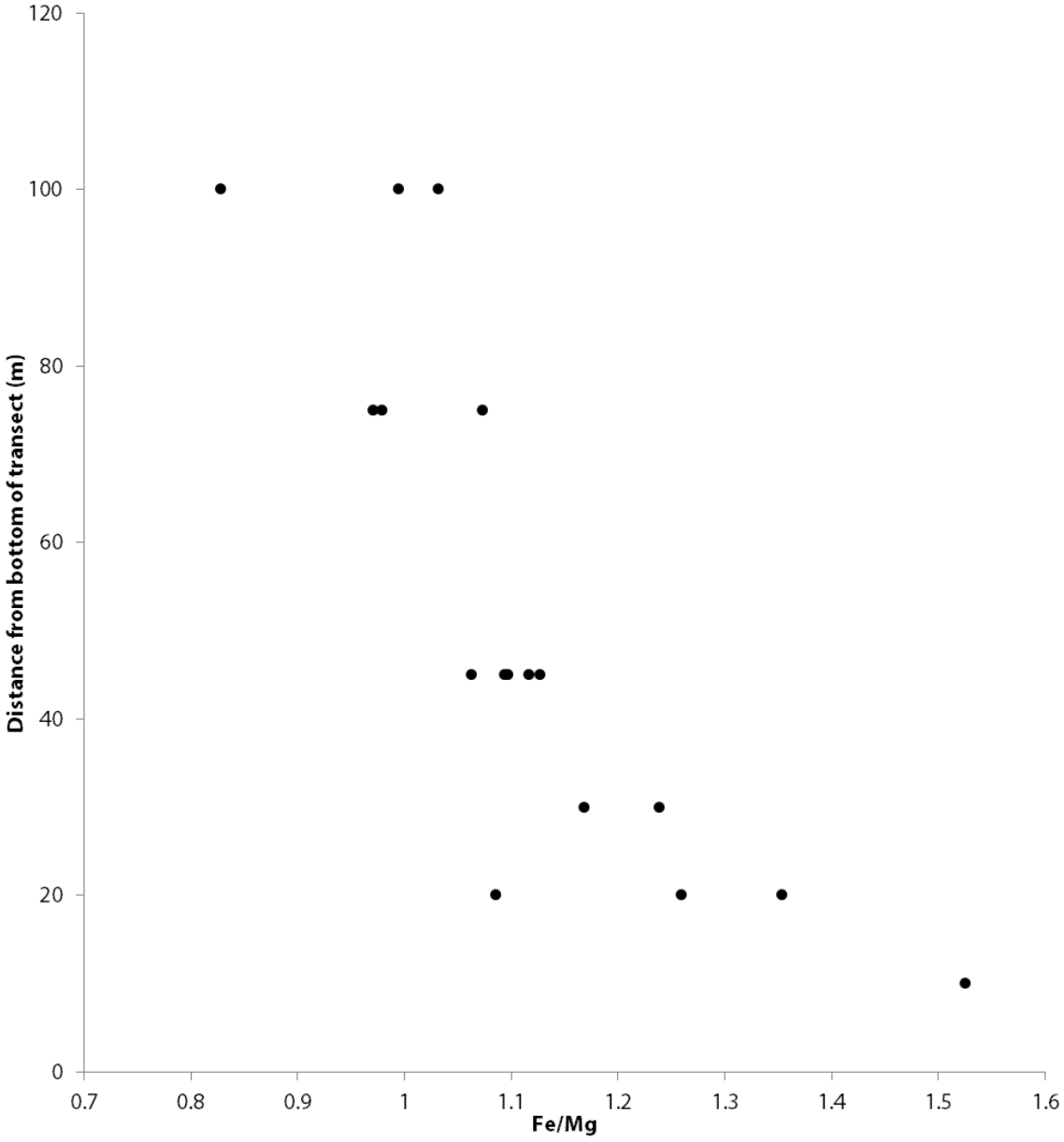

Figure 20: Muscovite compositions plotted against depth. Fe/Mg ratios systematically decrease from bottom to top of the transect. Compositions of chlorite porphyroblasts and chlorite in pressure shadows plotted against depth. Porphyroblasts consistently have lower Fe/Mg ratios with the exception of the topmost sample at 140 m, in which both porphyroblasts and pressure shadow chlorite reach a minimum Fe/Mg ratio.

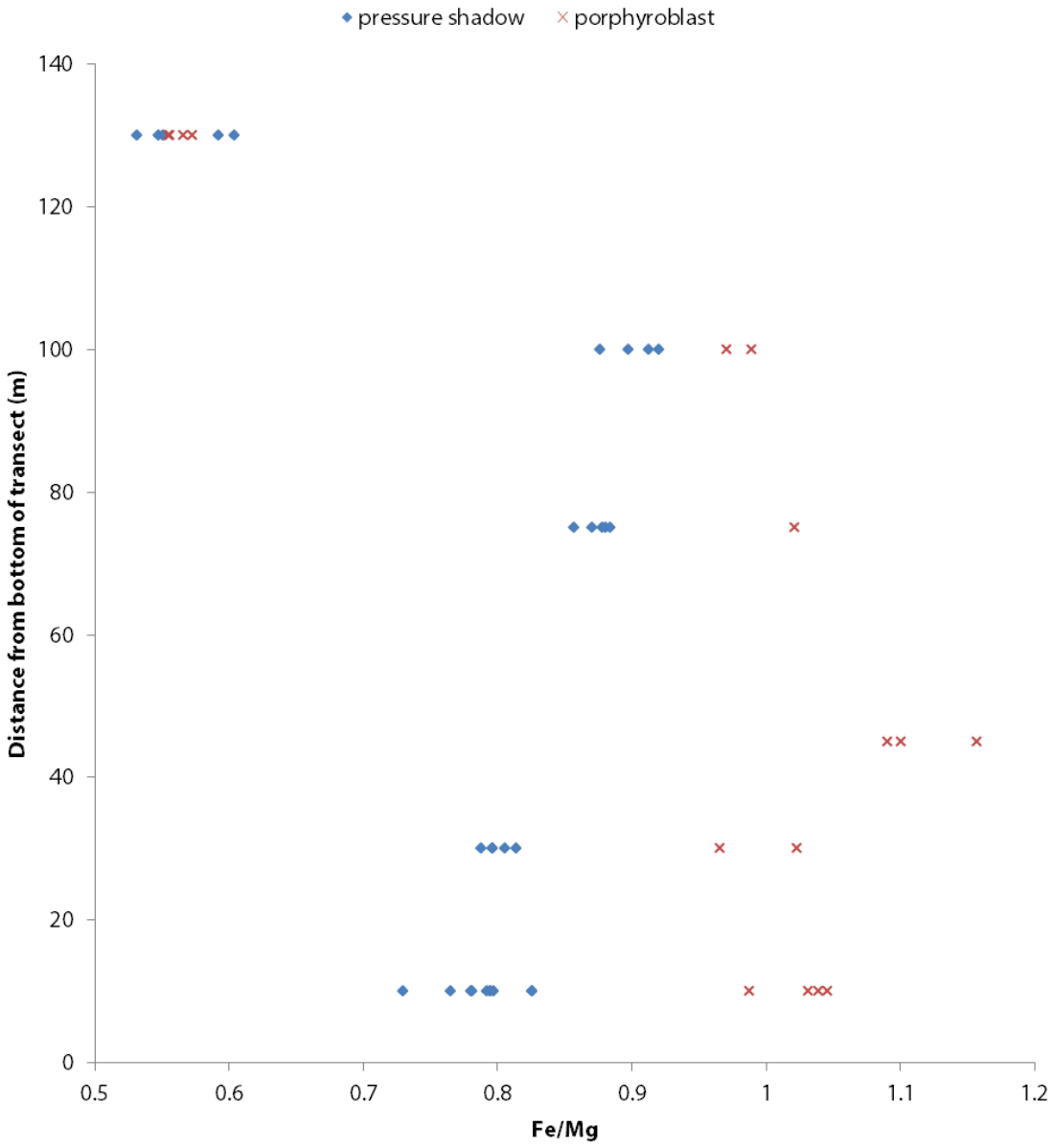

Figure 21: Compositions of chlorite porphyroblasts and chlorite in pressure shadows plotted against depth. Porphyroblasts consistently have lower Fe/Mg ratios with the exception of the topmost sample at 140 m, in which both porphyroblasts and pressure shadow chlorite reach a minimum Fe/Mg ratio.

Discussion

Mineral assemblages and textures confirm that a minimum of two episodes of footwall metamorphism affected all sampled sections of the footwall: (1) initial amphibolite facies metamorphism and (2) greenschist facies overprinting coeval with extension. Extensional deformation and textural disequilibrium of garnet and staurolite porphyroblasts show that amphibolite facies metamorphism was pre-kinematic relative to the extension-related deformation. Micas that appear to have grown at the expense of garnet and staurolite are aligned parallel to the axis of extension, which indicates that later, synkinematic, greenschist-facies metamorphism took place. Additionally, both prograde and retrograde generations of chlorite are present. Consistently higher Fe/Mg ratios distinguish late chlorite growth from chlorite porphyroblasts. This suggests that chlorite in pressure shadows formed at lower temperatures, consistent with greenschist facies retrograde metamorphism, and porphyroblasts formed during prograde metamorphism. Garnet zonation patterns in all samples are consistent with later retrogression of amphibolite-facies minerals; inflections in Mg and Mn zoning at the rims of garnets and pulled-apart garnet fragments are typical of retrogression during or after extension.

Although all samples experienced some retrogression, as evidenced by the presence of late chlorite and inflections of garnet zonation patterns throughout the entire transect, the top 30 m of the transect appears to have experienced the greatest amount of retrogression. Only garnets in this upper 30 m of the transect show distinctly Ca-depleted rims, which indicates that they experienced two distinct metamorphic events. In the study area, staurolite is not present in the top 30 m; however, chlorite in lenses of mica-quartz

aggregates here are texturally and compositionally similar to chlorite associated with staurolite breakdown in lower samples. This extensively retrogressed zone may then have contained an amphibolite facies assemblage before greenschist facies overprinting.

Linear trends in garnet and muscovite compositions with structural depth suggest that mineral chemistry is correlated with distance from the detachment, and that observed differences are due to differences in metamorphic conditions as opposed to differences in bulk composition. Both Fe/Mg ratios in chlorite and muscovite change systematically with depth, and Fe/Mg ratios in the structurally highest sample of the transect are significantly lower than in any other sample. Garnet and chlorite porphyroblasts also show compositional changes with depth; Fe/Mg ratios decrease with structural depth. As partitioning of Fe and Mg can change with metamorphic grade (e.g. Ferry & Spear, 1978; Spear, 1993), the existence of Fe/Mg trends with depth in garnet, chlorite, and muscovite are consistent with the observed metamorphic gradient with depth.

Synextensional fluid flow in the footwall may be responsible for retrogression of amphibolite-facies schists. Widespread breakdown of staurolite and garnet to chlorite and the abundance of high angle fluid inclusion planes in the structurally highest samples are interpreted as evidence for the presence of fluid during extension. The previous fluid flow study at Hendry's Creek by Gébelin et al. (2011) shows that localization of retrogression in samples nearest the detachment may be due to the influx of meteoric fluid along the NSRD; this previous study concluded that significant amounts of meteoric fluid were present in units above the structurally highest occurrence of staurolite-bearing schists (Fig. 22). In contrast with observations from lower structural levels, comparatively

extensive retrogression and high temperature compositions of retrograde minerals observed in samples nearest to the detachment are consistent with the presence of a hydrothermal system near the detachment.

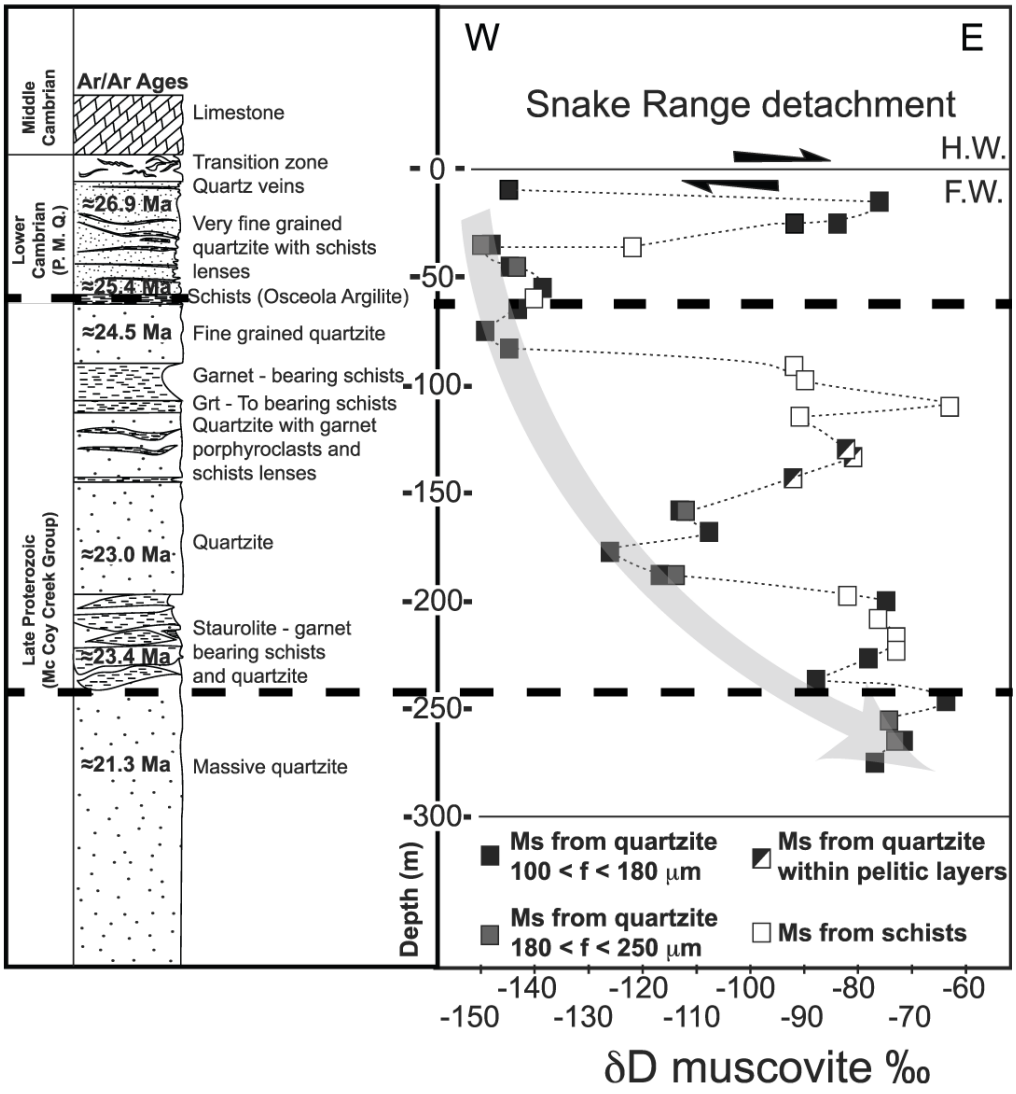

Figure 22: Isotope ratios from previous Hendry's Creek study on meteoric fluids. Samples above 188 m depth with lower δD muscovite values show evidence for the presence of meteoric water. Modified from Gébelin et al., 2010 to show the relative position of the Hendry's Creek transect from this study (bold dashed line).

Petrographic and mineral composition analyses indicate that all levels of the footwall of the NSRD initially experienced staurolite-zone metamorphism. A second, lower-grade metamorphic event coeval with Tertiary extensional deformation caused at least the top 100 m of footwall schist to retrogress to the chlorite-garnet zone. Petrographic textures signify that the presence of fluids near the top of the footwall during extension may have localized extensive retrogression to the highest levels of the footwall.

References

Armstrong, R.L., 1982, Cordilleran metamorphic core complexes - from Arizona to southern Canada: Annual Review of Earth and Planetary Sciences, v. 10, p. 129–154.

Bartley, J.M., and Wernicke, B.P., 1984, The Snake Range Décollement interpreted as a major extensional shear zone: Tectonics, v. 3, no. 6, p. 647–657, doi: 10.1029/TC003i006p00647.

Buck, W.R., 1988, flexural rotation of normal faults: Tectonics, v. 7, no. 5, p. 959–973, doi: 10.1029/TC007i005p00959.

Cooper, F.J., Platt, J.P., Platzman, E.S., Grove, M.J., and Seward, G., 2010a, Opposing shear senses in a subdetachment mylonite zone: Implications for core complex mechanics: Tectonics, v. 29, no. 4, p. n/a–n/a, doi: 10.1029/2009TC002632.

Cooper, F.J., Platt, J.P., Anczkiewicz, R., and Whitehouse, M.J., 2010b, Footwall dip of a core complex detachment fault: thermobarometric constraints from the northern Snake Range (Basin and Range, USA): Journal of Metamorphic Geology, v. 28, no. 9, p. 997–1020, doi: 10.1111/j.1525-1314.2010.00907.x.

Ferry, J.M. and Spear, F.S., 1978, Experimental calibration of the partitioning of Fe and Mg between biotite and garnet: Contributions to Mineralogy and Petrology, v. 66, p. 113-117.

Gans, P.B., Miller, E.L., Huggins, C.C. and Lee, J., 1999a, Geologic Map of the Little Horse Canyon Quadrangle, Nevada and Utah, Field Studies Map 20: Nevada Bureau of Mines and Geology, Reno, scale 1:24,000.

Gans, P.B., Miller, E.L. and Lee, J., 1999b, Geologic Map of the Spring Mountain Quadrangle, Nevada and Utah, Field Studies Map 18: Nevada Bureau of Mines and Geology, Reno, scale 1:24,000.

Gaudemer, Y., and Tapponnier, P., 1987, Ductile and brittle deformations in the northern Snake Range, Nevada: Journal of Structural Geology, v. 9, no. 2, p. 159–180, doi: 10.1016/0191-8141(87)90023-X.

Gébelin, A., Mulch, A., Teyssier, C., Heizler, M., Vennemann, T., and Seaton, N.C.A., 2011, Oligo-Miocene extensional tectonics and fluid flow across the Northern Snake Range detachment system, Nevada: Tectonics, v. 30, no. 5, p. n/a–n/a, doi: 10.1029/2010TC002797.

Hose, R.K., and Blake, M.C., 1976, Geology and Mineral Resources of White Pine County, Nevada, Part 1: Nevada Bureau of Mines and Geology Bulletin, v. 85, p. 1–32.

Lee, D., and Fischer, L., 1985, Cretaceous metamorphism in the northern Snake Range, Nevada, a metamorphic core complex: Isochron/West, v. 42, p. 3–7.

Lee, J., Miller, E.L., and Sutter, J.F., 1987, Ductile strain and metamorphism in an extensional tectonic setting: a case study from the northern Snake Range, Nevada, USA: Geological Society, London, Special Publications, v. 28, no. 1, p. 267–298, doi: 10.1144/GSL.SP.1987.028.01.18.

Lee, J., and Sutter, J.F., 1991, Incremental $^{40}Ar/^{39}Ar$ thermochronology of mylonitic rocks from the Northern Snake Range, Nevada: Tectonics, v. 10, no. 1, p. 77–100, doi: 10.1029/90TC01931.

Lee, J., 1995, Rapid uplift and rotation of mylonitic rocks from beneath a detachment fault: Insights from potassium feldspar $^{40}Ar/^{39}Ar$ thermochronology, northern Snake Range, Nevada: Tectonics, v. 14, no. 1, p. 54–77, doi: 10.1029/94TC01508.

Lee, J., Gans, P.B. and Miller, E.L., 1999a, Geologic Map of the Mormon Jack Pass Quadrangle, Nevada, pp. Field Studies Map 17: Nevada Bureau of Mines and Geology, Reno, scale 1:24,000.

Lee, J., Gans, P.B. and Miller, E.L., 1999b, Geologic Map of the Third Butte East Quadrangle, Nevada, Field Studies Map 16: Nevada Bureau of Mines and Geology, Reno, scale 1:24,000.

Lee, J., Miller, E.L., Gans, P.B. and Huggins, C.C., 1999c, Geologic Map of the Mount Moriah Quadrangle, Nevada, Field Studies Map 19: Nevada Bureau of Mines and Geology, Reno, scale 1:24,000.

Lewis, C.J., Wernicke, B.P., Selverstone, J., and Bartley, J.M., 1999, Deep burial of the footwall of the northern Snake Range decollement, Nevada: Geological Society Of America Bulletin, v. 111, no. 1, p. 39–51, doi: 10.1130/0016-7606(1999)111<0039.

Miller, E.L., Gans, P.B., and Garing, J., 1983, The Snake Range Décollement: An exhumed Mid-Tertiary ductile-brittle transition: Tectonics, v. 2, no. 3, p. 239–263, doi: 10.1029/TC002i003p00239.

Miller, E.L., Gans, P.B., Wright, J.E., and Sutter, J.F., 1988, Metamorphic history of the east-central Basin and Range province: Tectonic setting and relationship to magmatism, *in* Rubey Colloquium on Metamorphism and Crustal Evolution of the Western United States, Prentice-Hall, Englewood Cliffs, NJ, p. 649–682.

Miller, E.L., and Gans, P.B., 1989, Cretaceous crustal structure and metamorphism in the hinterland of the Sevier thrust belt, western U.S. Cordillera: Geology, v. 17, no. 1, p. 59–62, doi: 10.1130/0091-7613(1989)017.

Miller, E.L., Dumitru, T.A., Brown, R.W., and Gans, P.B., 1999, Rapid Miocene slip on the Snake Range–Deep Creek Range fault system, east-central Nevada: Geological Society of America Bulletin, v. 111, no. 6, p. 886–905, doi: 10.1130/0016-7606(1999)111<0886:RMSOTS>2.3.CO;2.

Miller, E.L. and Gans, P.B., 1999, Geologic Map of the Cove Quadrangle, Nevada, Field Studies Map 22: Nevada Bureau of Mines and Geology, Reno, scale 1:24,000.

Miller, E.L., Gans, P.B., Grier, S.P., Huggins, C.C. and Lee, J., 1999, Geologic Map of the Old Mans Canyon Quadrangle, Nevada, Field Studies Map 21: Nevada Bureau of Mines and Geology, Reno, scale 1:24,000.

Spear, F.S., 1993, Metamorphic Phase Equilibria and Pressure-Temperature-Time Paths: Mineralogical Society of America, Washington, D. C., 799 p.

Spencer, J.E., 1984, Role of tectonic denudation in warping and uplift of low-angle normal faults: Geology, v. 12, no. 2, p. 95–98, doi: 10.1130/0091-7613(1984)12.

Stewart, J., and Poole, F., 1974, Lower Paleozoic and uppermost Precambrian Cordilleran Miogeocline, Great Basin, Western United States: Tectonics and Sedimentation, v. 22, p. 28–57.

Wernicke, B., 1981, Low-angle normal faults in the Basin and Range Province: nappe tectonics in an extending orogen: Nature, v. 291, no. 5817, p. 645–648, doi: 10.1038/291645a0.

Wernicke, B., and Axen, G.J., 1988, On the role of isostasy in the evolution of normal fault systems: Geology, v. 16, no. 9, p. 848–851, doi: 10.1130/0091-7613(1988)016.

Whitney, D.L., and Seaton, N.C.A., 2010, Garnet polycrystals and the significance of clustered crystallization: Contributions to Mineralogy and Petrology, v. 160, no. 4, p. 591–607, doi: 10.1007/s00410-010-0495-1.

Appendix A. Sample coordinates and orientations

Sample	Strike	Dip	Lineation trend	Plunge	UTM coordinates
SR12-39	097	10	199	10	11S 51405 44848
SR12-38	355	08	120	08	11S 51381 44773
SR12-36	055	14	-	-	11S 51384 44762
SR12-33A	060	09	113	06	11S 50558 45370
SR12-33B	050	05	128	05	11S 50558 45370
SR12-34	343	15	114	13	11S 50574 45336
SR09-1B1	-	-	-	-	11S 50535 45312*
SR12-35	010	13	107	05	11S 50535 45312
SR12-32	085	18	122	16	11S 50556 45310

*approximate

Appendix B. Supplementary garnet X-ray maps

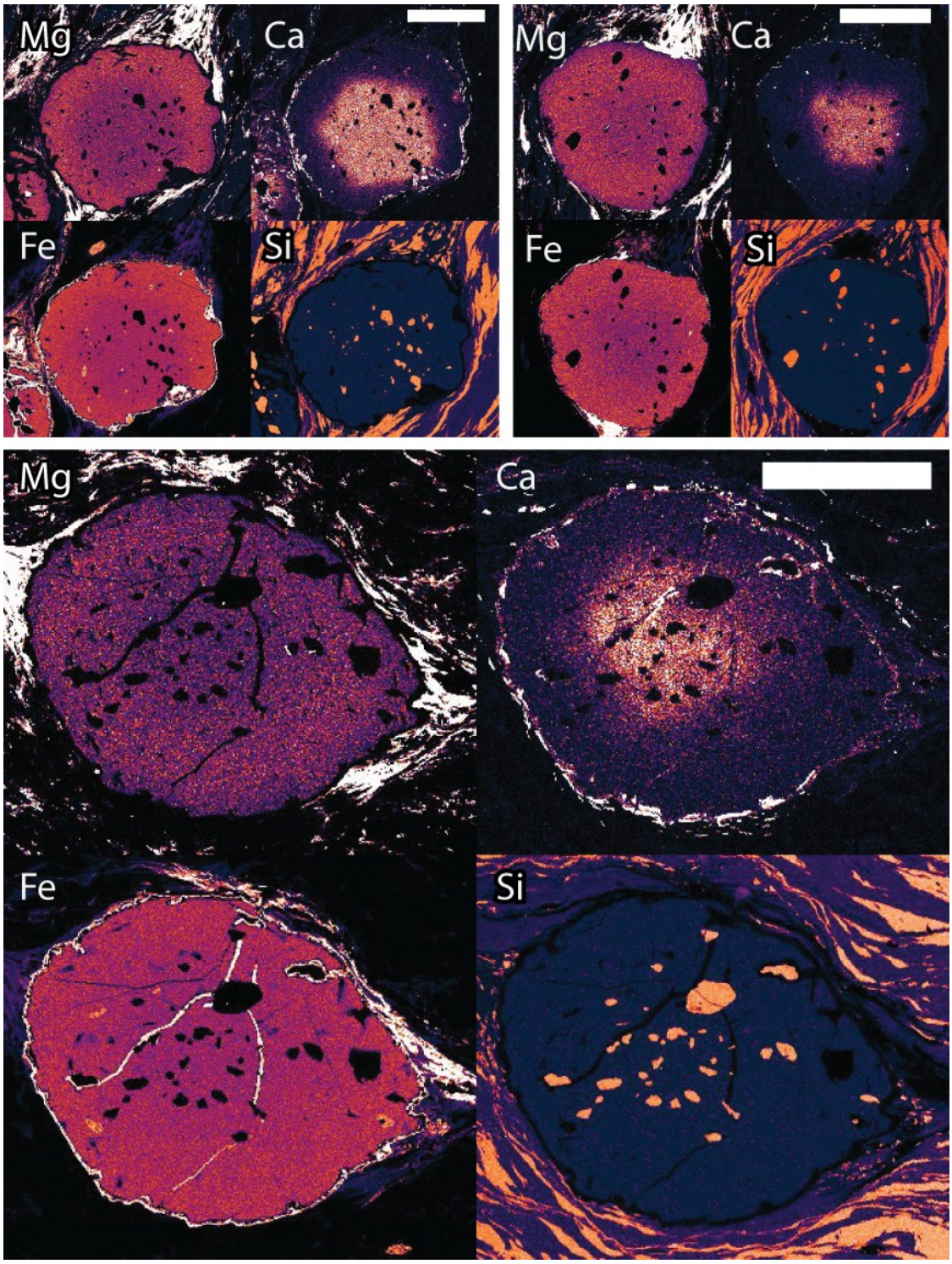

Figure A1: Garnet maps from sample SR12-38. White scale bars are 0.5 mm.

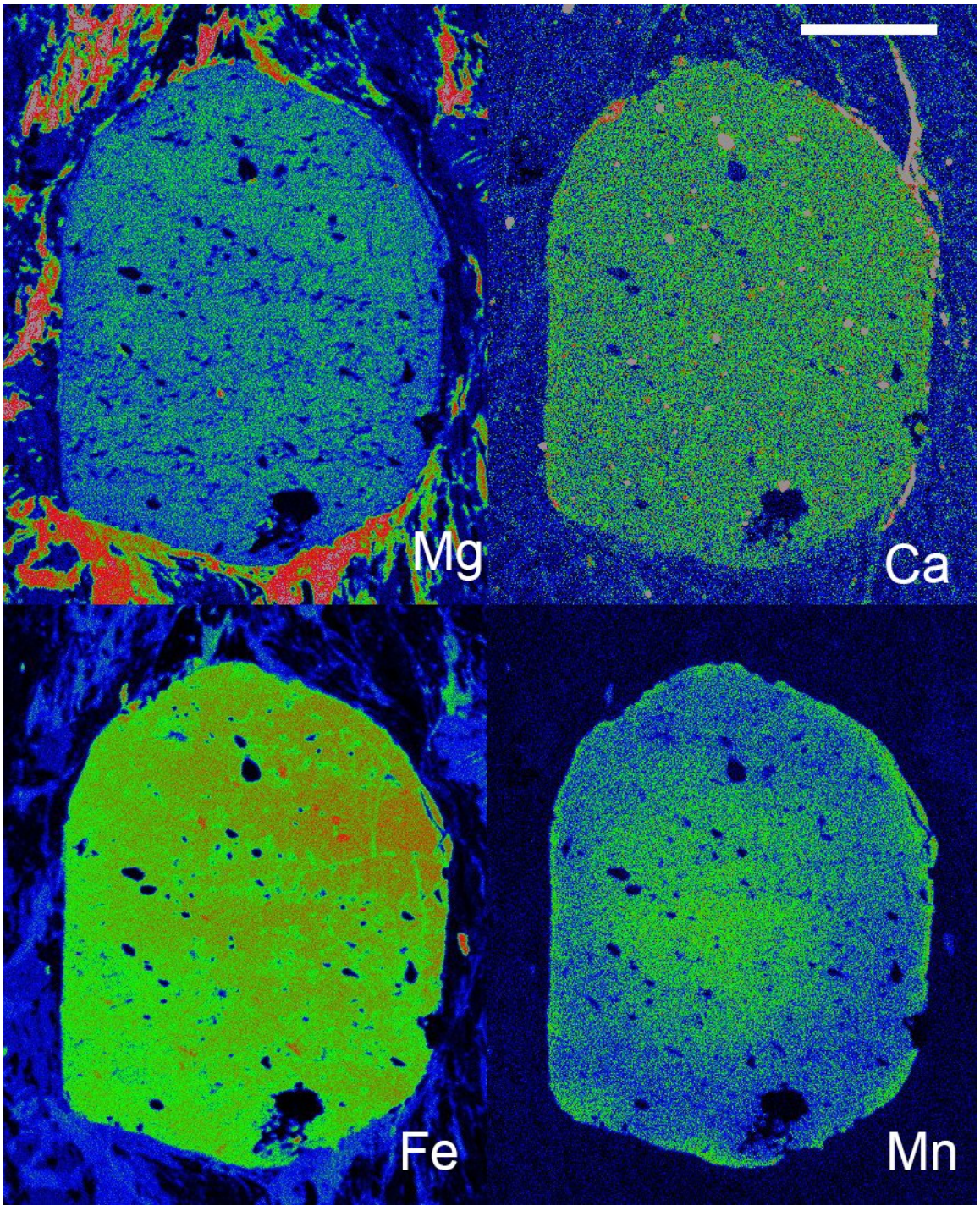

Figure A2: Garnet maps from sample SR12-36. White scale bar is 0.5 mm.

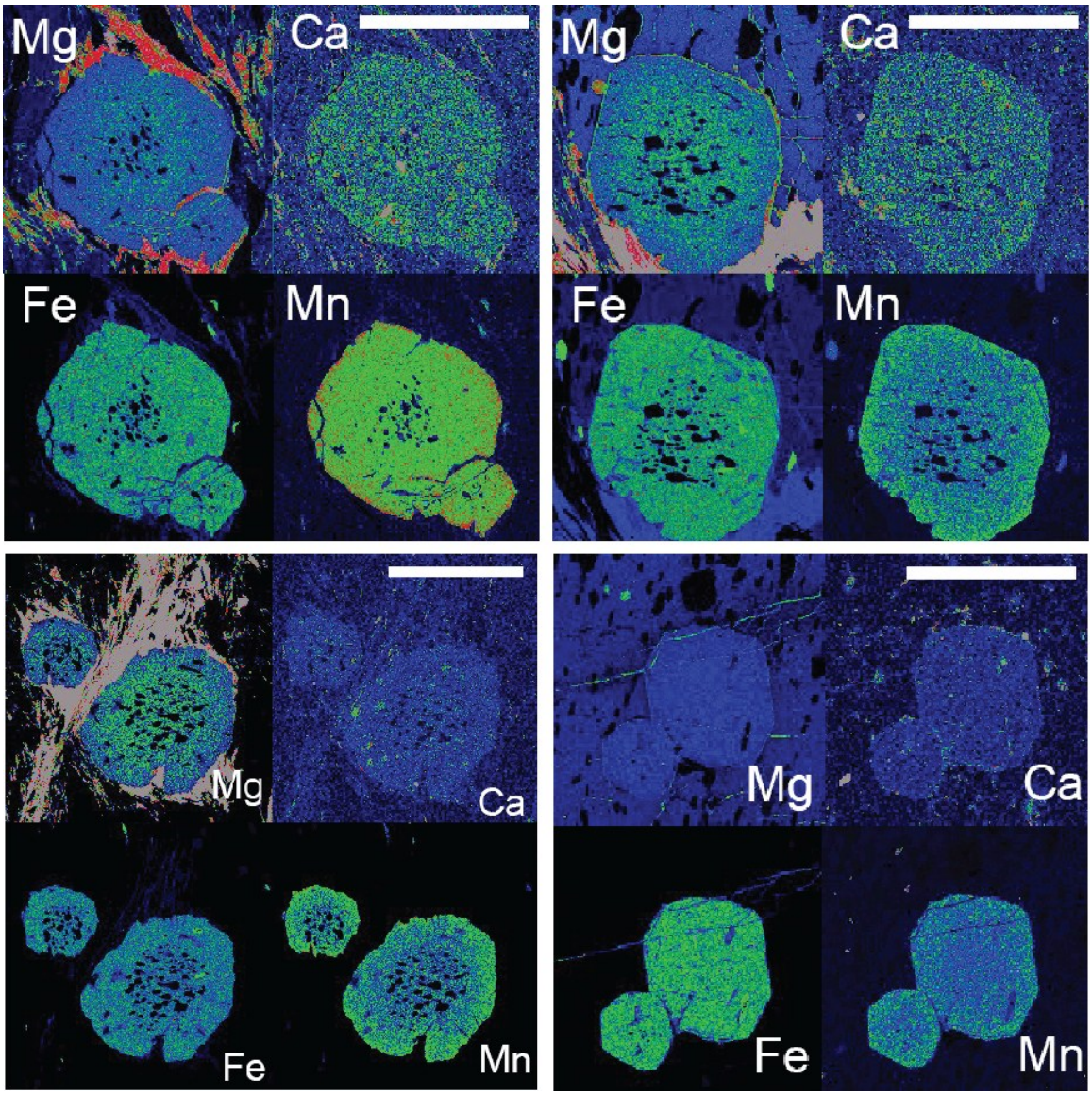

Figure A3: Garnet maps from sample SR12-33B. White scale bars are 0.5 mm.

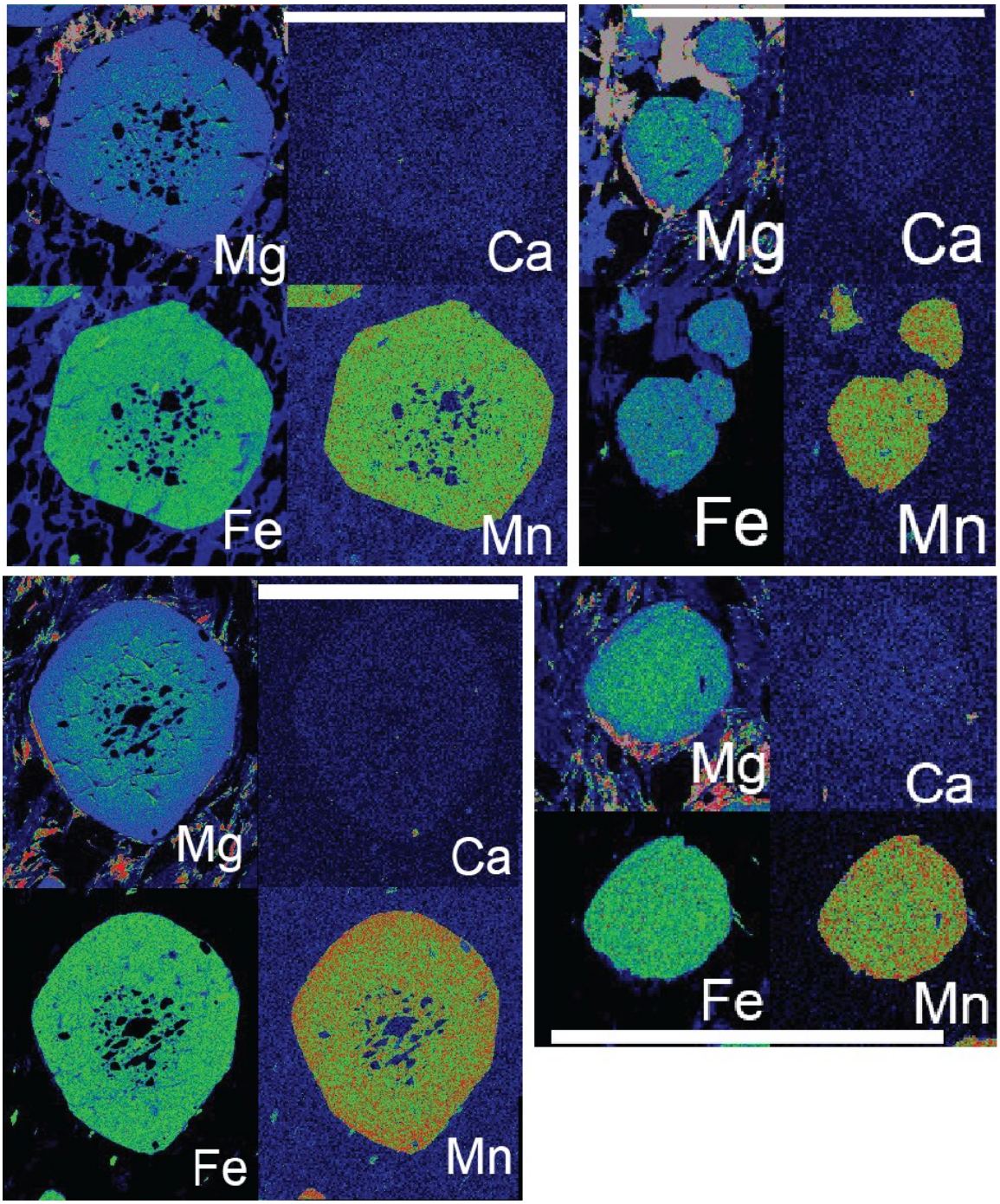

Figure A4: Garnet maps from sample SR12-33A. White scale bars are 1 mm.

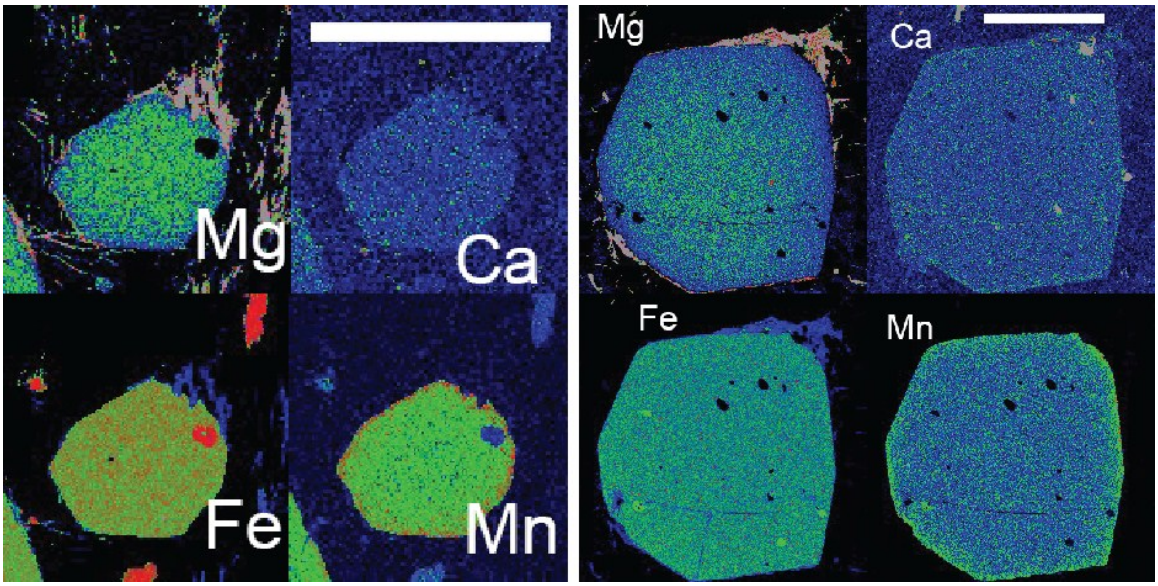

Figure A5: Garnet maps from sample SR12-34. White scale bars are 0.5 mm.

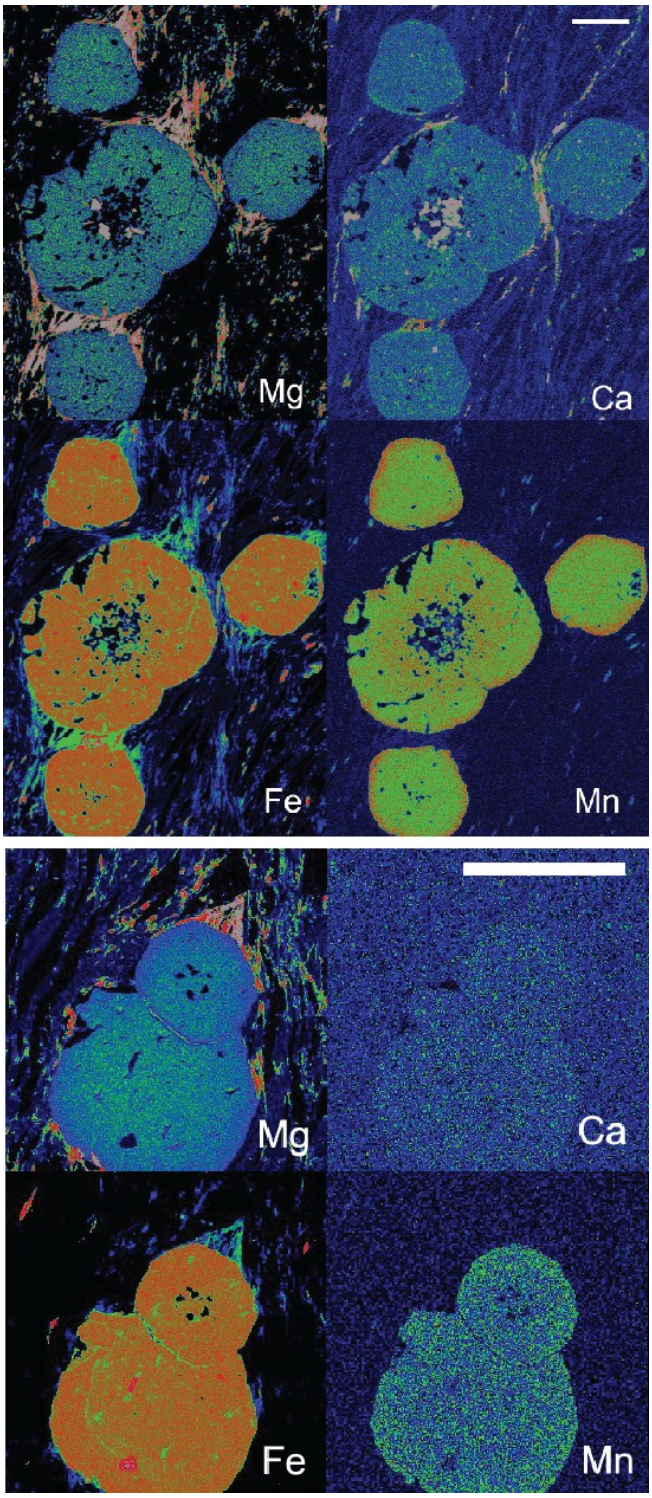

Figure A6: Garnet maps from sample SR12-35. White scale bars are 0.5 mm.

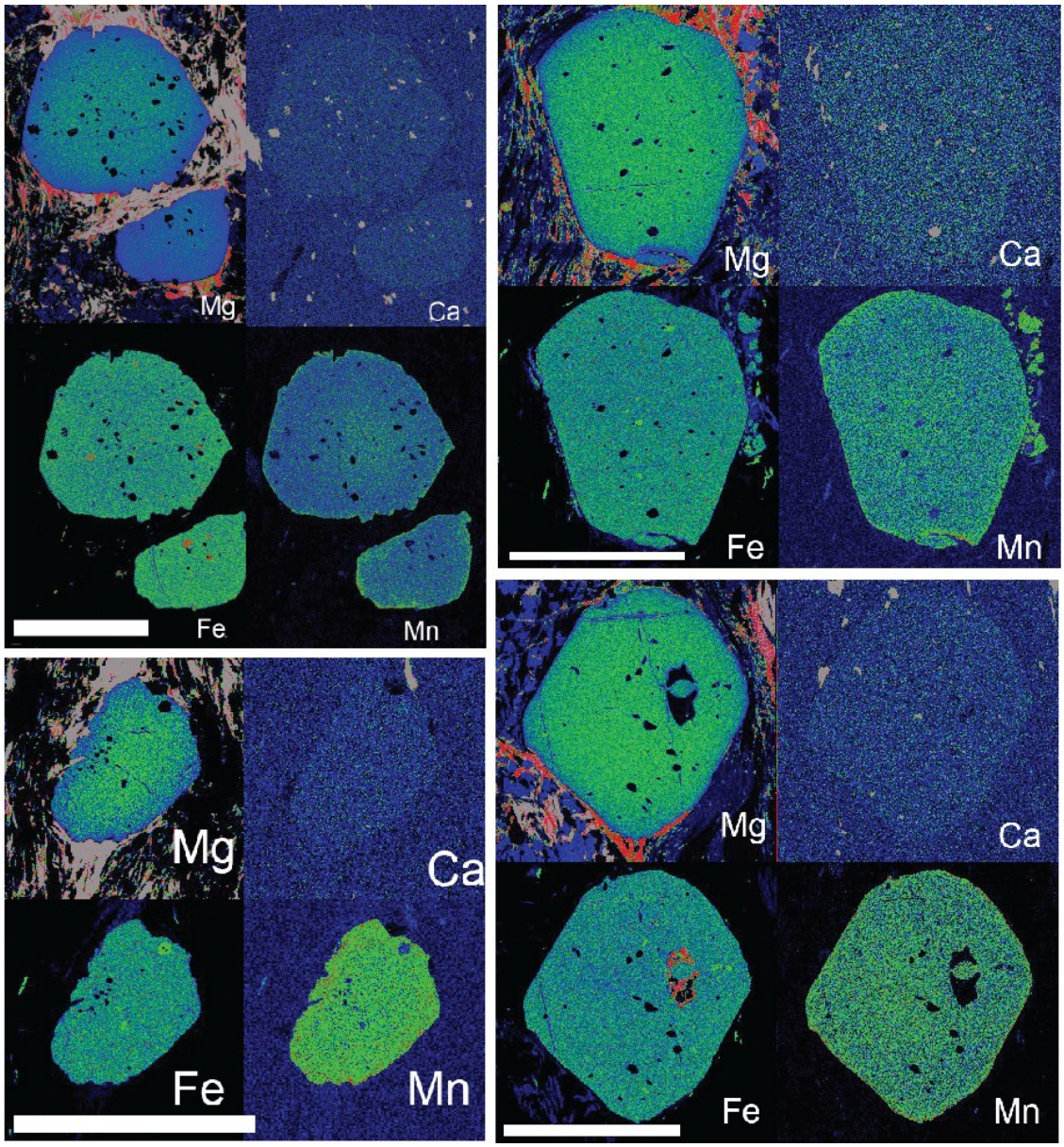

Figure A7: Garnet maps from sample SR12-32. White scale bars are 1 mm.